Edge and SOL turbulence and blob variations over a large database in NSTX

IOP Publishing | International Atomic Energy Agency Nuclear Fusion

Nucl. Fusion **55** (2015) 093035 (19pp) doi:10.1088/0029-5515/55/9/093035

Edge and SOL turbulence and blob variations over a large database in NSTX

S.J. Zweben[1], W.M. Davis[1], S.M. Kaye[1], J.R. Myra[2], R.E. Bell[1], B.P. LeBlanc[1], R.J. Maqueda[1,a], T. Munsat[3], S.A. Sabbagh[4], Y. Sechrest[3], D.P. Stotler[1] and the NSTX Team

[1] Princeton Plasma Physics Laboratory, Princeton, NJ 08540, USA
[2] Lodestar Research Corporation, Boulder, CO 80301, USA
[3] Department of Physics, University of Colorado, Boulder, CO 80309, USA
[4] Department of Applied Physics and Applied Mathematics, Columbia University, New York, NY 10026, USA

E-mail: szweben@pppl.gov

Received 5 February 2015, revised 5 June 2015
Accepted for publication 19 June 2015
Published 3 September 2015

Abstract

This paper describes the range of variations in edge and SOL turbulence observed using a gas puff imaging (GPI) diagnostic in NSTX discharges. The database consists of 140 shots including Ohmic, L-mode, and H-mode plasmas measured during steady-state conditions (e.g. without ELMs). Turbulence quantities were evaluated using both cross-correlation analysis and blob tracking. Relative fluctuation levels varied from $\delta I/I \sim 0.15$–1.0, correlation times were $\tau_{auto} \sim 15$–$40\ \mu$s, correlation lengths were $L_{pol} \sim L_{rad} \sim 5$–$10$ cm, and turbulence velocities were $V_{pol} \sim 2 \pm 1$ km s^{-1} and $V_{rad} \sim 0.5 \pm 0.5$ km s^{-1} outwards. These variations were evaluated with respect to both the global and local edge plasma parameters, and compared with simplified theoretical models.

Keywords: tokamak, turbulence, edge, scrape-off-layer

S Online supplementary data available from stacks.iop.org/NF/55/093035/mmedia

(Some figures may appear in colour only in the online journal)

1. Introduction

Edge and scrape-off-layer (SOL) turbulence is important in tokamaks because it affects the edge plasma profiles and the location of the plasma loss to the wall. The edge plasma profiles in turn affect the core plasma and fusion performance, and the location of heat and particle flux strongly influences the design of the divertor and first wall. Thus it would be useful to understand the existing variations in the edge and SOL turbulence in order to predict the edge transport in future devices.

The goal of this paper is to provide a detailed description of the observed variations in the edge and SOL turbulence in NSTX, a mid-sized spherical tokamak at PPPL [1]. The present analysis covers a wide database of turbulence measurements made during the steady-state periods of Ohmic, L-mode, and H-mode discharges. The specific motivation for this paper is to determine how edge turbulence varies with the global and local plasma parameters, how the turbulence characteristics are related to each other, and how well these turbulence variations can be described by simplified theoretical models.

To provide an introduction for the present paper, this section briefly summarizes prior review papers on this topic, and then summarizes the previous work in this area on NSTX. Further relationships between the present results and previous experimental results are discussed in each of the major sections of the paper.

[a] Presently at: X Science LLC, Plainsboro, NJ 08536 USA.

Two early reviews [2, 3] noted that the relative fluctuation level for various tokamaks increased with minor radius from $\tilde{n}/n < 0.01$ in the core to $\tilde{n}/n \sim 0.3$ at the edge, roughly consistent with the wave breaking (mixing length) limit $\tilde{n}/n \sim 1/k_{perp}L_n$, where k_{perp} is the radial wavenumber of the turbulence and L_n is the local density scale length. They also noted that the turbulence size scale was in the range $k_{perp}\rho_s < 1$, where k_{perp} is the perpendicular wavenumber and ρ_s is the drift-wave gyroradius parameter, and that the turbulence frequencies were in the range $\omega \sim k_{perp}v_{drift}$, where v_{drift} is the diamagnetic drift velocity. These results were roughly consistent with drift-wave turbulence theory, and these same theoretical characterizations of turbulence are still used in the discussion of the data in this paper.

A review paper several years later highlighted turbulence results from Ohmic discharges in TEXT [4]. The estimated turbulent convection in the SOL as measured by probes accounted for a significant fraction of the electron heat flux in the SOL, and a reversal of the poloidal velocity of the edge turbulence versus minor radius was found across the separatrix, but no satisfactory model was identified which predicted the measured features of edge turbulence. Subsequent reviews of turbulence and transport in toroidal devices highlighted progress in turbulence measurements, results from H-mode plasmas, and relationships to theory [5, 6]. A recent review of edge turbulence found the poloidal size scale range was $k_{pol}\,\rho_s \sim 0.02$–$0.1$, and noted some exceptions to the wave breaking fluctuation limit, e.g. the high fluctuation level in the flat density region in the far-SOL [7]. No clear plasma current or $q(a)$ scaling was found across machines, consistent with the similarity of edge turbulence in tokamaks, stellarators, and RFPs [5–7]. The most recent review of edge turbulence in tokamaks highlighted DIII-D results [8], and reiterated that a definitive scaling of edge turbulence with plasma or machine parameters has not yet been obtained.

Experimental results and theory of the discrete 'blob' structures seen in the edge of tokamaks and other devices were recently summarized in two extensive review papers [9, 10]. Tokamak blob sizes were ~0.5–4 cm (half-width), and radial blob velocities were ~0.2–3 km s^{-1}, bounded by the inertial and sheath-limited blob models (see section 6.4). Very recently, variations of edge turbulence from five stellarators and two tokamaks in L-mode showed systematic variations with the drift-wave parameters for both the edge and SOL, and outward blob transport in the SOL in all devices [11].

Now we summarize previous work in NSTX on edge turbulence as measured in steady-state conditions using GPI. The first results compared Ohmic, L-mode and H-mode plasmas and had some analysis of blobs [12]. Correlation lengths and turbulence velocities across the L–H transition were described for one plasma condition [13]. The intermittency in the SOL during H-modes was studied at power levels from $P_{NBI} = 0$–6 MW, with the lowest blob activity in Ohmic H-modes [14]. A scan of lithium coating resulted in a relatively small increase in edge turbulence velocity [15]. Most recently, the effect of the GPI gas puff itself was studied and little or no effect was seen on the edge plasma or edge turbulence at the peak of the GPI puff [16].

Table 1. Overall database parameters.

Number of shots	140
Plasma current	$I_p = 0.65$–1.15 MA
Toroidal field	$B_t = 3.5$–5.5 kG
Safety factor	$q_{95} = 5.8$–12.8
Elongation	$\kappa = 1.9$–2.5
Stored energy	$W_{mhd} = 26$–306 kJ
Average density	$n_e = (1.3$–$7.0) \times 10^{13}$ cm^{-3}
NBI heating	$P_{nb} = 0$–6 MW
RF heating	$P_{rf} = 0$–1.4 MW
Outer gap	2.8–15.7 cm
Lithium	0–370 mg/shot

Several theoretical analyses of the GPI results on NSTX have been published by the Lodestar group. The first paper [17] focused on a small set of blobs in L-mode and H-mode shots, and compared their radial motion with analytic blob models for convection. Subsequently, a reduced 2D edge turbulence simulation model was made using the SOLT code [18] and initial results were compared with fluctuation levels, blob structure, and heat flux SOL width measurements. A synthetic GPI diagnostic was added to SOLT [19] and further comparisons with GPI were made, including a sensitivity study with respect to various theoretical assumptions. Finally, SOLT simulations and GPI data were compared with respect to the effect of edge sheared flows on blobs [20], and detailed GPI blob tracking for one NSTX shot was interpreted in terms of edge shear flows.

The present paper describes the variations of edge turbulence and blobs in NSTX over a much larger database than previous papers. The outline is as follows: section 2 describes the database and data analysis methods, section 3 describes the turbulence and blob amplitudes, section 4 describes the turbulence and blob length scales, section 5 describes the turbulence and blob poloidal velocities, and section 6 describes the turbulence and blob radial velocities. Section 7 describes the turbulence and blob timescales, section 8 describes the multiple linear regression analysis, and section 9 contains the conclusions and suggested directions for further research.

Note that the present paper describes a very large database which contains several different turbulence variables, each evaluated at four different edge positions, along with many different plasma parameters, each evaluated for many NSTX discharges. Thus it is not possible to present a complete discussion of the database in this paper. However, the entire database, along with discharge parameters and sample GPI movies for each shot, is available on a web site for further investigation [21].

2. Database and data analysis

2.1. Database selection

The database used in this paper contains 140 discharges from the 2010 NSTX run, each of which had a single deuterium GPI gas puff during the constant-current period of the shot. The range of global plasma parameters is given in table 1. All discharges were made in deuterium with a major radius

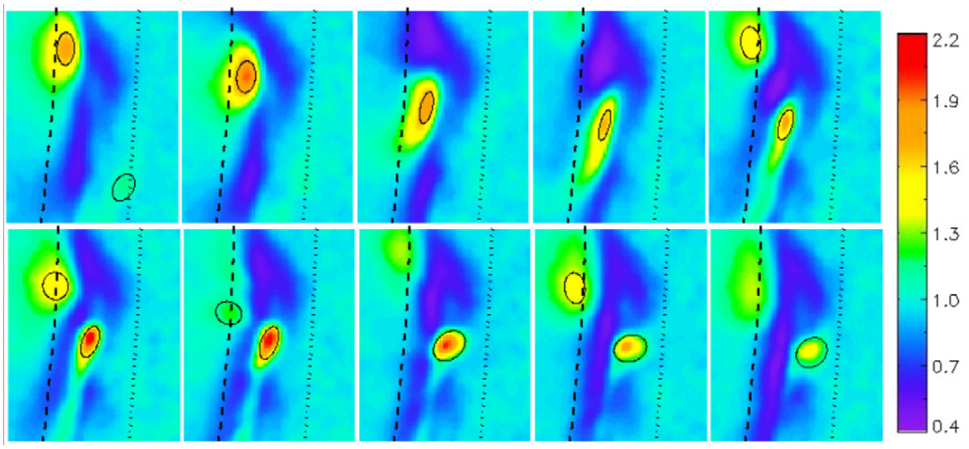

Figure 1. Sample images of the normalized GPI Dα light emission versus time for a typical H-mode shot during 4 MW of NBI (#140395). The time between these images is 10 μs (4 frames) and their size is ~30 cm poloidally (vertical) × 24 cm radial (horizontal). Each image is normalized to the time-averaged image, and the relative fluctuation levels are shown by the colour scale on the right. The location of blobs (defined in the text) is shown by the elliptical regions. The magnetic separatrix is the dashed line and the shadow of the limiter (RF antenna) is the dotted line (an online movie is linked here) (stacks.iop.org/NF/55/093035/mmedia).

$R \sim 85$ cm, minor radius $a \sim 65$ cm, carbon plasma-facing surfaces with lithium conditioning, a toroidal magnetic field on axis of $B_t = 3.5$–5.5 kG, and a plasma current of $I_p = 0.65$ –1.15 kA (1 kG = 0.1 Tesla). This database includes shots from about 17 separate experiments covering most of the range of NSTX operation. Of these 140 shots, 93 were in H-mode (all with NBI), 33 were Ohmic, and 14 in L-mode (9 with NBI only and 5 with RF). All shots had an elongated magnetic equilibrium with $\kappa \sim 1.9$–2.5 and $q_{95} = 5.8$–12.8, with nearly all shots (135/140) having a lower single-null divertor shape. The five shots (all H-modes) with a shape nearer to double-null or upper-single-null were still within the EFIT reconstruction uncertainty of a lower single-null shape, and all the edge and SOL turbulence properties for these five shots were similar to those with a clear lower-single-null shape.

The turbulence was analysed during a 10 ms period centred at the peak of the GPI gas puff in these discharges. The shots used in the database were selected by the following criteria, which were applied from 10 m before to 5 ms after the peak of the GPI Dα signal: constant plasma current, toroidal field, and applied heating power; absence of large MHD activity such as ELMs or large coherent MHD modes; absence of L–H or H–L transitions; good GPI signal levels (GPI gas puff ~3–6 Torr l); appropriate B field-line angle for GPI viewing along B (i.e. $I_p/B_t = 0.2 \pm 0.05$ MA kG^{-1}); constant outer separatrix position to within ±1 cm, with at least 3 cm inside the separatrix visible within the GPI field of view; and GPI data taken at the fastest available camera rate (397 660 frames s^{-1}). About 45% of the shots taken at this GPI framing rate satisfied the other conditions. This database included some shots which were used previously for GPI analysis of the turbulence velocity versus lithium [15], the gas puff effects of GPI [16], and comparisons of GPI with SOLT [20]. The entire database, along with discharge parameters and sample GPI movies for each shot, is available on a web site for further investigation [21].

2.2. Gas puff imaging diagnostic

The present NSTX GPI diagnostic is the same as described recently [16]. A fast Phantom 710 camera viewed a 30 cm poloidal by 24 cm radial region in the plane perpendicular to the local B field just above the outer midplane near the separatrix. A gas manifold was attached to the nearby wall and puffed deuterium gas into this region, and the Dα light from the neutral deuterium from this puff is viewed through a 657 nm (9 nm FWHM) optical filter at 397 660 frames s^{-1} using an 80 × 64 pixel array. The integration time for each frame was 2.1 μs, the time between frames was 2.5 μs, and the spatial resolution of the optical system was ~0.5 cm at the GPI gas cloud.

Sample images of the normalized GPI Dα light emission versus time are shown in figure 1 for a typical H-mode shot with 4 MW of NBI (#140395). The time between these 64 × 80 pixel images is ~10 μs (i.e. 4 time frames), and they are oriented so that the poloidal direction is approximately vertical (with the ion diamagnetic direction down), and the radial direction is approximately horizontal (outwards to the right). The EFIT magnetic separatrix is the dashed line, and the shadow of the limiter (RF antenna) is the black dotted line in each frame. The relative amplitude of the local fluctuations in each image is normalized to the time-averaged of all images averaged over 1 ms, with the normalized amplitude shown by the colour scale. The location of discrete blobs in each frame (defined in section 2.4) is shown by the black ellipses.

Although the GPI data is digitized for ~80 ms per shot, the data in this paper focuses on time periods within ±5 ms of the peak GPI gas puff rate, which includes 4000 frames (i.e. 40 MB of data per shot). This is the time of the maximum GPI signal level (typically 20 times the pre-puff Dα level), and also a time when the perturbation of the gas puff on the edge plasma was found to be negligible [16]. Typical camera signals levels are ~500–1500 counts per pixel in the region of maximum brightness in these 12 bit camera images.

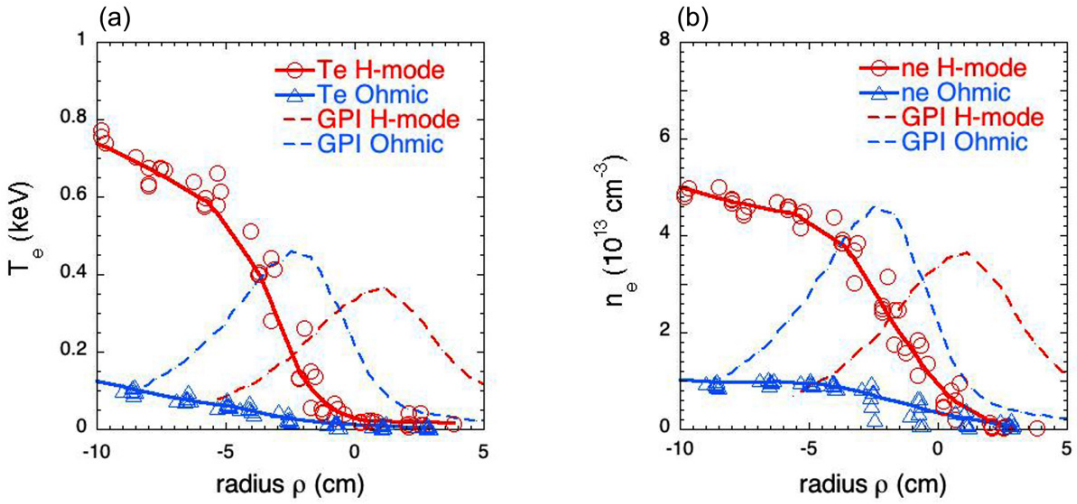

Figure 2. Measured Thomson scattering data for the (*a*) electron temperature and (*b*) density for two sub-sets of this dataset: one Ohmic group and one H-mode group with 4 MW of NBI. Each plot contains data from 7 similar shots with the parameters defined in table 2. Overlaid with the Thomson data is the radial profile of the GPI Dα light emission for these cases (same in both panels). All curves are plotted with respect to the separatrix as determined from the EFIT equilibrium reconstruction code.

2.3. Sample edge profiles

Sample profiles of edge electron temperature and density derived from Thomson scattering data are shown in figures 2(*a*) and (*b*). These plots show the results from 7 similar Ohmic shots (with no NBI) and 7 similar H-mode shots (with 4 MW of NBI). This data was taken near the time of peak GPI signal, and is plotted with respect to the outer midplane separatrix determined from the EFIT equilibrium reconstruction code. The shot-to-shot variations in the midplane separatrix position were within 0.5 cm for both H-mode and Ohmic groups. The maximum variation of the separatrix position for reconstructions of nearby equilibria were 0.73 cm for the H-mode cases and 0.21 cm for the Ohmic cases. Therefore, in these cases and in general, the accuracy of the EFIT separatrix position is estimated to be about ±1 cm.

Overlaid in both figures 2(*a*) and (*b*) are the radial profiles of the GPI Dα light emission signals (in arbitrary units) for typical shots in these series (#140389 and 141746). The GPI signal levels peaked within about ±2 cm of the separatrix in these cases, and normally have usable data over ±4 cm around the separatrix. Note that similar GPI Dα profiles and their absolute magnitude were previously well fit by DEGAS 2 modelling based on Thomson data in H-mode plasmas [22].

A summary of the plasma and edge parameters for these shots is in table 2, along with the estimated local ρ_s, τ_{ei}, and β_e at 2 cm inside the separatrix (i.e. $\rho = -2$ cm), using the magnetic field on axis B_t to evaluate ρ_s and β_e. The average electron temperatures 2 cm inside the separatrix were $T_e \sim 134$ eV for H-mode and $T_e \sim 23$ eV for Ohmic plasmas, and near the separatrix they were $T_e \sim 29$ eV for H-mode and $T_e \sim 13$ eV for Ohmic. Thus there was a significant difference in temperature (and density) between these sample plasmas, which cover a bit less than the range of edge parameter variations in this database.

2.4. Turbulence and blob analysis methods

Edge turbulence cross-correlation and blob-tracking analysis was done for each of the 140 shots in the GPI database of table 1. These analyses were averaged over ±5 ms around the peak of the GPI signal, during which time the turbulence quantities were checked to be nearly constant. The methods used in these analyses, which are similar to those used in [16], are described in this section, and the results are described in sections 3–8.

The turbulence cross-correlation analysis method used time series of the GPI signal from small regions of the image to calculate the local fluctuation levels, turbulence correlation lengths, and turbulence velocities. These analyses average over the entire spectrum of turbulence size scales and timescales, i.e. this method does not track individual 'blob' structures. These time series were derived from averaging over 4 × 4 pixels (1.5 cm × 1.5 cm) near the vertical middle of the GPI images, i.e. over regions much smaller than the correlation lengths of the turbulence. These local correlation analyses were centred at four different radii with respect to the separatrix; namely, $\rho = -2$ cm, 0 cm +2 cm and +4 cm. The point at $\rho = -4$ cm was not analysed, since for some shots (with large outer gaps) that region was at the edge of the GPI view.

The relative GPI fluctuation levels $\delta I/I$ (standard deviation/mean) were calculated from standard statistics, and the autocorrelation times (FWHM) were calculated from time-delayed cross-correlation functions. The correlation lengths L_{pol} and L_{rad} (FWHM) were calculated using the zero-time-delay cross-correlation coefficient C_{12} between two 4 × 4 pixel time series separated by $\delta x_{12} = 2.4$ cm in either the poloidal or radial direction from the centre of the locations used to calculate $\delta I/I$. The correlation lengths were estimated assuming a Gaussian spatial cross-correlation function to be $L_{12} = 1.66\delta x_{12}/(-\ln C_{12})^{1/2}$. These correlation lengths were constant over the analysis time, and averaged over this time

Table 2. Sample plasma parameters.

	H-mode	Ohmic
Shot range	140389–395	141746–756
Time (s)	0.532	0.215
I_p (kA)	830	830
B_t (kG)	4.9	3.6
W_{mhd} (kJ)	220	32
n_e (10^{13} cm^{-3})	5.2	1.6
P_{nb} (MW)	4.0	0
T_e (0) (eV)	920	530
n_e (0) (10^{13} cm^{-3})	5.6	2.3
T_e (a) (eV)	29 ± 17	13 ± 6
n_e (a) (10^{13} cm^{-3})	0.92 ± 0.54	0.37 ± 0.23
T_e @ −2 cm (eV)	134 ± 53	23 ± 4
n_e @ −2 cm (10^{13} cm^{-3})	2.1 ± 0.47	0.47 ± 0.17
ρ_s (cm) @ −2 cm	0.3	0.2
τ_{ei} (μs) @ −2 cm	1.5	0.5
β_e @ −2 cm	0.005	0.0003

for use in the database. Note that the radial correlation lengths are *local* estimates at each of the chosen radii, and when these radial correlation lengths are large compared with plasma parameters scale lengths (as they sometimes are), this does not imply that the turbulence is constant over the whole radial correlation length.

The turbulence velocities were estimated from the time-delayed cross-correlation functions between time series from individual pixels separated either radially or poloidally. Starting from a single pixel at a given ρ at the vertical middle of the GPI image, a search was made within the 2D region of ±20 pixels poloidally and ±10 pixels radially for the pixel which had the highest cross-correlation coefficient with the starting pixel, given a 1 frame time delay between the two time series. The same process was repeated for 2, 3, and 4 frame time delays, i.e. up to a 10 μs time delay, at which time the maximum cross-correlation coefficients were typically 0.8 ± 0.1. The poloidal and radial locations of these correlation peaks versus their time delay were fit by a straight line to derive the poloidal and radial turbulence velocities.

The blob tracking analysis was done using a completely different method [20, 23]. Figure 1 showed examples of the blob tracking done for this data. All frames are first normalized by a 1 ms time-average of all frames, in order to identify the relative local maxima in each frame, i.e. the blobs. For the present analysis, a blob is identified when the maximum of the normalized signal is larger than an assumed value of 1.5. The region around each of these maxima is then fit by contours, and an ellipse is fit to the half-maximum contour level. The motion of the central maximum and the shape and tilt of the elliptical fits are then tracked from frame-to-frame. The maximum allowed displacement of a given blob between frames limited to 10 pixels (3.8 cm) to help distinguish different blobs. These blob structures and motions are saved in the database only if they meet these criteria and can be continuously tracked for a lifetime of more than 15 μs. Note that by this (arbitrary) definition a blob can be either inside or outside the separatrix, and that this method does not search for negative perturbations ('holes').

Blobs are tracked this way over the entire image, and the results were binned within 2 cm wide regions centred at the same radii as for the turbulence analysis, namely: $\rho = -2$ cm, 0 cm +2 cm and +4 cm. The blob quantities calculated for each shot were the average number of blobs per frame N_{blob}, the normalized blob amplitudes A_{blob}, the poloidal and radial sizes scales of the blobs L_{pol} and L_{rad} (FWHM), and the poloidal and radial blob velocities V_{pol} and V_{rad}. These database quantities were averaged over all blobs detected within the 10 ms period of interest for each shot.

2.5. Interpretation of GPI turbulence analysis

As discussed previously [24], the measured GPI signal is due to the excitation of the deuterium Dα line, and depends on at least three factors: the local deuterium neutral density, the local electron density, and the local electron temperature. The time-averaged 2D spatial distribution of the GPI Dα light emission has been calculated using the 3D Monte Carlo simulation DEGAS, and the resulting 2D distribution and magnitude of Dα agree well with the time-averaged Dα light in quiescent H-mode discharges [22].

However, the measured GPI fluctuations cannot be directly interpreted in terms of the local electron density or temperature fluctuations without some additional assumptions. Thus the turbulence analyses in sections 3–8 are done using the GPI Dα signal itself, and do not try to interpret those results in terms of the plasma density or temperature fluctuations. The best way to compare these Dα analyses with respect to theory or simulation is to convert the theoretical turbulence into 'synthetic' GPI signals using the well-known dependences of Dα on the neutral density and electron density and temperature. This has been done previously when such theoretical turbulence predictions were available, for example in [20, 25, 26]; however, turbulence simulations of NSTX are were not available for all shots this database.

Nevertheless, some approximate interpretations of the GPI signals can be made. We can assume that where and when the GPI signal level was increased by over a factor-of ×10 due to the GPI gas puff (as it was for all the shots in this paper), the local neutral density is dominated by the GPI gas puff. Since the neutral gas influx rate from the GPI puff is constant over turbulence times scales, we will assume that the fluctuations in the GPI signal are dominated by the local electron density and temperature fluctuations. This neglects possible 'shadowing' or modulation of the local neutral density by the local electron density and temperature fluctuations [24], which tends to be most important radially inside the peak of the Dα emission.

Thus we will assume that the observed fluctuations in the GPI Dα signal are dominated by the local electron density and temperature fluctuations. If these n_e and T_e fluctuations are highly correlated with each other, as predicted from edge turbulence theory [20, 25, 26], then the local Dα fluctuations should have a simple relationship to the local electron density fluctuations. For example, if the Dα light emission intensity is parametrized as $I = n_o n_e^{\alpha} T_e^{\beta}$, where n_o is the neutral deuterium density, then for small fluctuations

Table 3. Average edge parameters at $\rho = -2$ cm versus shot type and Dα exponents.

Shot type	Shots	NBI + RF (MW)	T_e@ −2 cm (eV)	n_e@ −2 cm (10^{13} cm^{-3})	α exponent (for n_e)	β exponent (for T_e)
Ohmic	33	0	25 ± 8	0.57 ± 0.18	0.80 ± 0.05	0.6 ± 0.2
L-mode	14	0.8	34 ± 17	0.87 ± 0.42	0.75 ± 0.05	0.4 ± 0.2
H-mode	93	3.5	122 ± 72	2.5 ± 1.4	0.65 ± 0.10	0.1 ± 0.2

$\delta I/I = \alpha(\delta n_e/n_e) + \beta(\delta T_e/T_e)$. If δn_e and δT_e are in phase, then the relative intensity fluctuations $\delta I/I$ are linearly proportional to $\delta n_e/n_e$, with a proportionality constant which depends on α, β, and $\delta n_e/\delta T_e$. If δn_e and δT_e are not in phase, then the resulting δI is a mixture of these two fluctuations, and more difficult to interpret. Separate probe measurements of δn_e and δT were made together in the SOL of an L-mode plasma in ASDEX Upgrade which showed $\delta n_e/n_e \gg \delta T_e/T_e$ [27], suggesting that $\delta I/I$ in GPI depends more on density than temperature fluctuations; however, such probe measurements were not available in NSTX.

If $I \sim n_e^{\alpha}$, then there is a direct relationship between the correlation properties of I and n_e. For example, it was shown numerically that the cross-correlation of a random variable to some power $-2 < \alpha < 4$ is very nearly the same as the cross-correlation of that variable itself [12]. In this case the correlation times, lengths and velocities calculated using cross-correlation functions of GPI light intensity should be the same as those of the density fluctuations, independent of α. This is intuitively clear from our experience with the nonlinear contrast knob on TV monitors; the basic structure and motion of objects does not change when the contrast exponent ('gamma') is changed.

Table 3 shows the Dα exponents α and β for the average electron temperatures and densities for various types of shots in this database at $\rho = -2$ cm. The density exponent were $\alpha \sim 0.65$–0.8 and the temperature exponent were $\beta \sim 0.1$–0.6 at this radius. In general, over $T_e \sim 5$–200 eV, $\alpha \sim 0.9$–1.0 for $n_e < 10^{12}$ cm^{-3} and $\alpha \sim 0.6$–0.9 for $n_e = 10^{12}$ cm^{-3}–2×10^{13} cm^{-3}. Also, β is nearly independent of density over $n_e = 10^{12}$ cm^{-3} – 10^{13} cm^{-3}, and monotonically increases with temperature from $\beta \sim 0.0$–0.1 at $T_e \sim 100$ eV to $\beta \sim 1$ at $T_e \sim 10$ eV. Thus possible electron temperature fluctuations are less significant for GPI in the higher temperature regions. It should be kept in mind that the practical usefulness of these α and β for interpreting the GPI results is limited due to the large fluctuation levels in edge n_e and T_e, especially in the SOL, and due to the unknown ratio of $\delta n_e/n_e$ to $\delta T_e/T_e$.

3. Turbulence and blob amplitudes

This section describes the edge and SOL turbulence and blob fluctuation amplitudes for this database. Section 3.1 describes the turbulence analysis results, i.e. the fluctuation amplitudes derived from cross-correlation analysis. Section 3.2 describes the blob amplitudes, i.e. those derived from the discrete structures. Section 3.3 discusses theoretical interpretations, and section 3.4 describes the relationship of these results to previous experiments.

3.1. Turbulence amplitudes

The radial profiles of relative GPI Dα fluctuation levels derived from cross-correlation analysis are shown in figure 3(*a*), sorted according to discharge type, and with error bars showing the shot-to-shot standard deviations. The fluctuation levels increase from $\delta I/I \sim 0.15$–0.3 at $\rho = -2$ cm inside the separatrix to $\delta I/I \sim 0.6$–1.0 at $\rho = +2$ and +4 cm outside the separatrix, and there was a significantly lower fluctuation level in H-mode compared to Ohmic or L-mode, except at $\rho = +4$ cm.

Three examples of the relative fluctuation levels versus the global plasma parameters are shown in figures 3(*b*)–(*d*), along with the approximate ranges of Ohmic and H-mode plasmas shown as dashed lines. Figure 3(*b*) shows that the relative fluctuations decrease with increasing line-averaged density at $\rho = \pm 2$ cm, as indicated by power law fits with exponents −0.55 ± 0.05. Figure 3(*c*) shows the relative fluctuation levels also decrease with increased plasma stored energy W_{mhd}, with power law exponents −0.35 ± 0.05. Figure 3(*d*) shows the relative fluctuation levels at $\rho = \pm 2$ cm also decrease with respect to the lithium coating applied just before the shot, fit here by straight lines. Similar trends were seen at $\rho = 0$ cm, but almost no variations of the relative fluctuation level were seen at $\rho = +4$ cm.

The variation of the relative fluctuation levels with the edge T_e and edge pressure gradient evaluated at $\rho = -2$ cm (from Thomson scattering) are shown in figures 3(*e*) and (*f*). The $\delta I/I$ variation with T_e was fit by a power law with exponent −0.3 ± 0.05, and the $\delta I/I$ variation with edge pressure gradient was fit by a power law with exponent −0.15 ± 0.05, although there were no clear variations within Ohmic plasmas alone, or within H-mode plasmas at $\rho = -2$ cm. Similar variations of the relative fluctuation levels with edge T_e and grad P_e were seen at $\rho = 0$ cm, but less variation was seen at $\rho = +4$ cm.

Table 4 shows linear (pair-wise) correlation coefficients between the turbulence amplitudes $\delta I/I$ (top row) and several of the discharge parameters in this database. For clarity only results for $\rho = \pm 2$ cm are shown, and only the most significant correlations (above 0.5) are indicated. Significant correlations occur between $\delta I/I$ and neutral beam power P_{nb}, stored plasma energy W_{mhd}, line-averaged density (n_e-ave), lithium per shot, and edge n_e. Table 4 also shows a moderate (53%) correlation between the turbulence amplitudes and the toroidal field B_t, but there were no significant turbulence correlations with I_p (not shown).

Table 5 shows the power-law exponents obtained from the fits of the turbulence fluctuation levels with the parameters in table 4, with entries only for cases with a linear

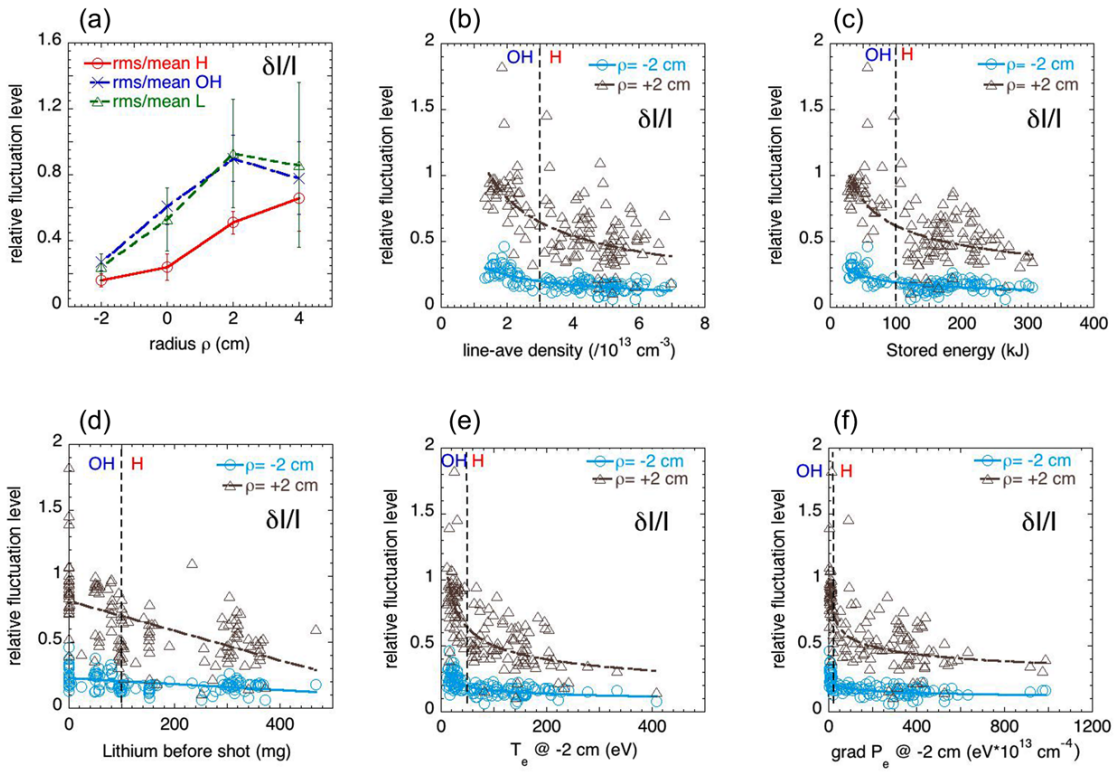

Figure 3. (*a*) shows the relative turbulence fluctuation levels versus the radius with respect to the separatrix, sorted according to discharge type. (*b*)–(*d*) show the variations of the relative fluctuation levels at $\rho = \pm 2$ cm with the global line-averaged density, plasma stored energy, and lithium applied before the shot. (*e*) and (*f*) show the variations of the relative fluctuation levels at $\rho = \pm 2$ cm with the local edge temperature and edge pressure gradient at 2 cm inside the separatrix. The approximate parameter ranges for Ohmic and H-mode shots are indicated by the vertical lines.

Table 4. Linear (pair-wise) cross-correlation coefficients.

	Radius	B_t	P_{nb}	W_{mhd}	n_e-ave	Li/sh	Edge n_e	κ
$\delta I/I$	−2 cm	0.53	0.57	0.63	0.69	—	0.62	—
	+2 cm	—	0.66	0.63	0.63	0.54	0.64	—
τ_{auto}	−2 cm	—	0.61	0.60	0.65	—	—	—
	+2 cm	—	—	—	—	—	—	—
L_{pol}	−2 cm	—	0.65	0.65	0.61	0.52	0.55	0.53
	+2 cm	—	—	0.54	—	0.51	—	0.55
L_{rad}	−2 cm	—	—	—	0.54	—	0.61	—
	+2 cm	—	—	—	—	—	—	—
V_{pol}	−2 cm	—	0.63	0.69	0.68	0.59	0.53	—
	+2 cm	—	—	—	—	—	—	—
V_{rad}	−2 cm	—	—	—	—	—	—	—
	+2 cm	—	—	—	—	—	—	—

cross-correlation >0.5. For example, the relative fluctuation levels at $\rho = -2$ cm decreased with the line-averaged density $\delta I/I \sim n_e^{-0.52}$, as also seen in figure 3(*a*), and with W_{mhd} as $\delta I/I \sim n_e^{-0.32}$. The P_{nb} correlations of figure 4 were not fit by a power law due to the zero values for Ohmic plasmas.

Here and elsewhere in this paper we find significant correlations of the turbulence properties with two or more plasma parameters which are also correlated with each other; for example, $\delta I/I$ in table 4 is highly correlated with n_e-ave and W_{mhd}, which also have a high cross-correlation with each other (79%), and there is also a high correlation between the edge T_e, n_e, and grad P_e. Furthermore, at least some (but not all) of these correlations are associated with the change from Ohmic to H-mode plasmas, as illustrated in figures 3(*b*) and (*c*). Thus it is not possible at present to determine which is the most important single parameter which controls these turbulence variations. Indeed, the turbulence is most likely determined by the local dimensionless physics parameters, as discussed for example in section 3.3.

3.2. Blob amplitudes

Figures 4(*a*) and (*b*) show the radial profiles of average number of blob (per frame per shot) N_{blob} and average blob amplitudes A_{blob} (normalized to the average signal level) derived from blob tracking analysis, sorted according to discharge type. Each point includes all blobs within ±1 cm of that radial position (e.g. from −3 cm to −1 cm for $\rho = -2$ cm). Note that the peak of 0.4 blobs/frame corresponds to 1600 blobs detected for that shot within the time period of interest (±5 ms around the peak of the GPI signal).

Figure 4(*a*) shows that very few blobs were identified inside the separatrix for H-mode plasmas, but that the number of blobs per zone was similar for all types of shots at $\rho = +2$ cm and +4 cm outside the separatrix. The normalized blob

Table 5. Power law exponents for linear cross-correlations.

	Radius	B_t	W_{mhd}	n_e-ave	Li/shot	Edge n_e	κ
$\delta I/I$	−2 cm	−1.7 ± 0.29	−0.32 ± 0.03	−0.52 ± 0.05	—	−0.30 ± 0.03	—
	+2 cm	—	−0.39 ± 0.04	−0.61 ± 0.07	−0.12 ± 0.02	−0.37 ± 0.03	—
τ_{auto}	−2 cm	—	0.39 ± 0.03	0.62 ± 0.05	—	—	—
	+2 cm	—	—	—	—	—	—
L_{pol}	−2 cm	—	0.37 ± 0.03	0.55 ± 0.05	0.09 ± 0.01	0.29 ± 0.04	2.92 ± 0.04
	+2 cm	—	0.23 ± 0.03	—	—	—	2.42 ± 0.31
L_{rad}	− 2 cm	—	—	0.64 ± 0.07	—	0.36 ± 0.04	—
	+ 2 cm	—	—	—	—	—	—

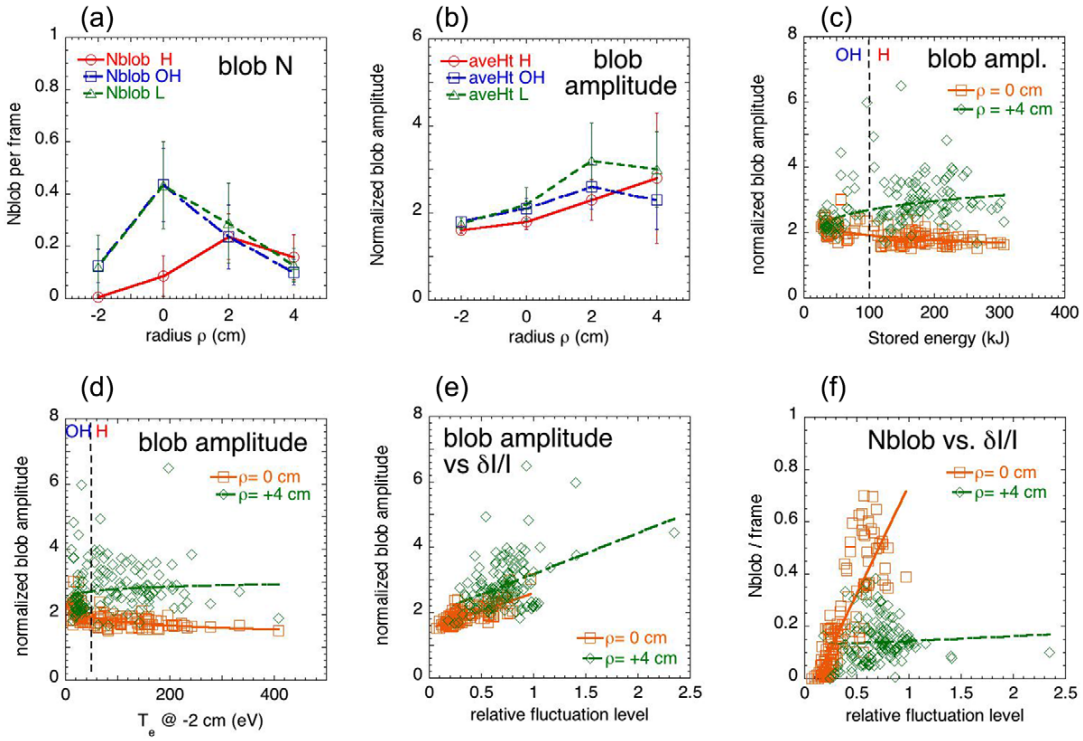

Figure 4. (*a*) and (*b*) show radial profiles of the average number of blobs per frame and the normalized blob amplitude, sorted according to shot type. (*c*) and (*d*) show the blob amplitude versus the plasma stored energy and edge temperature for $\rho = 0$ cm and +4 cm type (the minimum normalized amplitude for a blob is 1.5 in these units). (e) and (f) show the blob amplitude and blob number versus the relative turbulence fluctuation level for $\rho = 0$ cm and +4 cm.

amplitude as shown in figure 4(*b*) generally increased from inside to outside the separatrix for all types of discharges, with the average amplitude just above the blob detection threshold of 1.5 inside the separatrix. The average blob amplitude at $\rho = 2$–4 cm was ~2.5–3 for all types of shots.

Since there were relatively few blobs detected at $\rho = -2$ cm for H-modes, examples of blob statistics will be presented for $\rho = 0$ cm and +4 cm. Figure 4(*c*) shows that the normalized blob amplitudes decrease slightly with W_{mhd} at $\rho = 0$ cm, and increase slightly with W_{mhd} at $\rho = +4$ cm. Figure 4(*d*) shows that the blob amplitudes are largely independent of the edge T_e at $\rho = 0$ cm and +4 cm. These blob amplitude variations at $\rho = -2$ cm and +2 cm (not shown) are similar to those at $\rho = 0$ cm and +4 cm, respectively. The relationship between blob amplitudes and the relative turbulence levels from correlation analysis are shown in figure 4(*e*). The normalized blob amplitude is well correlated with the $\delta I/I$ fluctuation level at both $\rho = 0$ and +4 cm (and at $\rho = \pm 2$ cm). The number of blob at $\rho = 0$ cm is well correlated with $\delta I/I$, but almost independent of $\delta I/I$ at $\rho = +4$ cm.

3.3. Turbulence amplitudes versus theory

It is somewhat surprising that the turbulence amplitudes of section 3.1 decrease with increasing density, stored energy, edge T_e and edge pressure gradient, since the free energy available for turbulence drive generally increase with these quantities. In this section we compare the measure

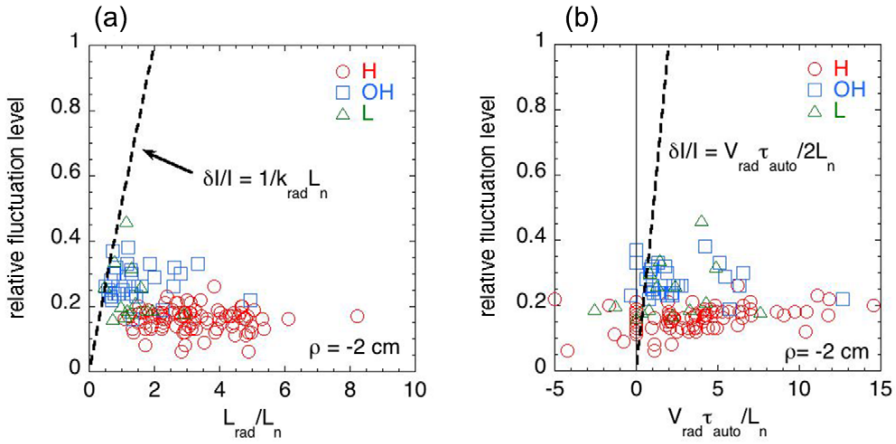

Figure 5. Comparison of the measured relative fluctuation level $\delta I/I$ at $\rho = -2$ cm with simplified theoretical models. (*a*) shows that Ohmic and L-mode shots are near the expected wave-breaking (mixing length) limit of $\delta I/I \sim L_{\rm rad}/2L_n$, but that H-mode shots are well below this limit. (*b*) shows that the Ohmic and L-mode fluctuation levels are near the expected interchange limit of $\delta I/I \sim V_{\rm rad}\,\tau_{\rm auto}/2L_n$, but that H-mode shots are well below this limit.

turbulence amplitude variations with two simple theoretical models.

The nonlinear saturation level expected for turbulent fluctuations due to the generic 'wave-breaking' mechanism is $\delta n/n \sim 1/k_{\rm rad}L_n$, independent of the type of linear instability, where L_n is the local density gradient scale length and $k_{\rm rad}$ is the turbulence radial wavenumber. Figure 5(*a*) shows a test of this relationship at $\rho = -2$ cm assuming $\delta I/I = \delta n/n$ (see below) and $k_{\rm rad} = 2/L_{\rm rad}$, where $L_{\rm rad}$ is the radial scale length from correlation analysis (see section 4). Most of the Ohmic and L-mode shots are near this wave-breaking limit with $\delta I/I \sim (0.5\text{–}1)L_{\rm rad}/2L_n$. However, the measured fluctuation levels for the H-mode shots are $\delta I/I \sim (0.06 - 0.3)L_{\rm rad}/2L_n$, i.e. much smaller than expected from the wave-breaking limit, and also apparently independent of $L_{\rm rad}/L_n$. This relationship could not be tested at larger radii since the local density gradient scale lengths were not well known there.

Alternatively, the nonlinear saturation level for interchange turbulence is due to the radial convection of fluid motion [28, 29], i.e. $\delta n/n = \delta V_{\rm rad}/\omega L_n$, where ω is a typical frequency of the turbulence and $\delta V_{\rm rad}$ is the radial velocity fluctuation. Assuming that $\delta I/I = \delta n/n$ (see below), $\delta V_{\rm rad} = V_{\rm rad}$ (see section 6), and $\omega \sim 2/\tau_{\rm auto}$ (see section 7), the database results for $\rho = -2$ cm are plotted in figure 5(*b*). The observed fluctuation levels are close to this limit in Ohmic plasmas, but smaller than this limit by a factor of ~2–8 in H-mode plasmas, similar to the results of figure 5(*a*). However, in general $L_{\rm rad}$ is not well correlated with $V_{\rm rad}\tau_{\rm auto}$, so these two plots in figure 5 are not identical, and in some shots the measured $V_{\rm rad}$ is zero or negative, not at all consistent with this scaling.

Note that the relative fluctuation levels $\delta I/I$ used for figure 5 can be converted to $\delta n/n$ using the expected variation of the Dα light emission $\delta I/I = \alpha\ \delta n/n$, where $\alpha \sim 0.65$–0.80 for the range of $n_{\rm e}$ and $T_{\rm e}$ used for these plots (see table 3). Thus for example the density fluctuation level in H-mode discharges at $\rho = -2$ cm corresponding to $\delta I/I \sim 0.15$ would be $\tilde{n}/n \sim 0.25$. However, this would not significantly change the qualitative results, and would still leave unresolved the possible Dα dependence on $\delta T_{\rm e}$, since the ratio $\delta T_{\rm e}/\delta n$ is not known.

The results of figure 5 should be considered only an approximate or qualitative comparison of experiment and theory. However, the large difference between these models and the measured H-mode fluctuation levels implies that this theoretical prediction and these measurements do not match very well. This may in part be due to an overestimation of $L_{\rm rad}$ for H-mode cases, or perhaps the turbulence in H-mode plasmas is determined by other physics outside these models, such as the flow shear, which was not characterized in this database.

3.4. Comparison with previous experiments

The large relative fluctuation level in the edge and SOL and its increase with minor radius across the separatrix has been seen in many previous tokamaks using Langmuir probes and scattering techniques [2–8]. The turbulence amplitudes of section 3.1 are similar to previous NSTX GPI results, including those done using He I emission instead of Dα [12]. For example, fluctuation levels previously seen ~4 cm outside the separatrix in H-mode plasmas were near unity and independent of NBI power from ~2–6 MW [14]. The present database did not include cases where very small edge and SOL fluctuation levels were observed in Ohmic H-mode plasmas [14], or during the transient 'quiet periods' seen just before the L–H transition [30].

Beam emission spectroscopy measurements (BES) in NSTX of edge turbulence in the steep-gradient region of MHD-quiescent H-mode plasmas [31, 32] showed relative fluctuation levels of $\delta n/n \sim 0.01$–0.05, which is significantly smaller than the $\delta n/n \sim 0.25$ inferred for GPI results in a similar radial region of $\rho = -2$ cm (see section 3.3). Parameter scaling in this BES data included an increase in $\tilde{n}$/n with dn/dr and $1/L_n$, whereas GPI data for H-modes at $\rho = -2$ cm did not show significant trends in these directions. A detailed comparison of

the BES and GPI measurements within the same discharges on NSTX was presented elsewhere [33]. Langmuir probe measurements in L-modes and H-modes in NSTX [34] showed relative density fluctuation levels increasing from ~0.1 just inside the separatrix to ~0.5–1.0 in the SOL, which were similar to those in figure 3(*a*). Measurements by microwave reflectometry ~1 cm inside the separatrix in NSTX [35] showed a decrease in edge density fluctuations from $\delta n/n \sim 0.2$ to <0.01 with increased lithium coating, whereas the GPI fluctuation at $\rho = -2$ cm in figure 3(*d*) decreased from ~0.2 down to ~0.1 (on average) with increased lithium coating.

The relative fluctuation level in the ion saturation currents in Langmuir probes in MAST increased from ~0.4 at 1 cm inside the separatrix to ~0.8 at 4 cm outside the separatrix [36], similar to the GPI fluctuation levels in figure 3(*a*). These probe result also agreed at least qualitatively with numerical simulations of interchange instability done with the ESEL code, although possible effects of electron temperature fluctuations were noted. The GPI diagnostic and probes on Alcator C-Mod also shows similar edge fluctuation levels as in figure 3(*a*) [37].

There have been several previous studies of edge turbulence scaling within a single tokamak. For example, the edge density fluctuation levels $\tilde{n}/n$ did *not* vary with ρ_s/L_n or the local density at a fixed radius in Ohmic TEXT plasmas [38], similar to results here at $\rho = -2$ cm (not shown in the figures). In DIII-D [39] the relative density in blobs (a.k.a. 'IPO's') normalized to the local plasma density in the SOL in L-mode plasmas was fairly constant versus line-averaged density. In the present paper the average blob amplitude and relative fluctuation level at $\rho = +4$ cm were both constant versus plasma density over all regimes (to within the scatter), consistent with the DIII-D results. However, at $\rho = 0$ cm both the blob amplitudes and relative fluctuation levels decreased with increased density, while at $\rho = +2$ cm both the blob amplitudes and relative fluctuation levels decreased slightly with increased density (e.g. figure 3(*b*)). For example, at $\rho = 0$ cm, the relative fluctuation level decreased from $\delta I/I \sim 0.6$ at $n = 1.5 \times 10^{13}$ cm^{-3} to $\delta I/I \sim 0.2$ at $n = 7 \times 10^{13}$ cm^{-3}, while the average blob amplitude decreased from $A_{blob} \sim 2.2$ to 1.6. In general, the relative fluctuation level increases with both A_{blob} and N_{blob}, as shown in figures 4(*e*) and (*f*), but the exact relationship between these experimental measures depends in detail on the choice of threshold condition for the definition of a blob; note that this blob threshold condition is different for the DIII-D paper [39] and the present paper.

Langmuir probe measurements in the lower divertor SOL of ASDEX-Upgrade in upper-X-point discharges showed the relative density fluctuation level to be nearly the same in L-mode and H-mode [40], which is similar to the far-SOL results in figures 3 and 4. Studies of blobs done in the SOL of L-mode plasmas in ASDEX-Upgrade using a lithium-BES diagnostic [41] showed that blobs, as defined by a conditional sampling criterion, had a relative fluctuation level $\delta I/I \sim 0.1$–0.6 and depended only weakly on B_t, which is similar to the blob results of section 3.2. The blob detection rate in the far-SOL as measured recently by GPI in ASDEX-Upgrade did not vary substantially between L-mode and H-mode [42], which is similar to the blob number results shown for $\rho \geqslant 2$ cm in figure 4(*a*).

4. Turbulence and blob length scales

This section describes the edge and SOL turbulence and blob scale lengths for this database. Section 4.1 describes the turbulence lengths derived from cross-correlation analysis. Section 4.2 describes the scale lengths derived for the blob structures. Section 4.3 discusses theoretical interpretations, and section 3.4 describes the relationship of these results to previous experiments.

4.1. Turbulence scale lengths

The radial profiles of the poloidal and radial turbulence scale lengths L_{pol} and L_{rad} (FWHM) from cross-correlation analysis are shown in figures 6(*a*) and (*b*), sorted according to shot type, with error bars giving the shot-to-shot standard deviations. For Ohmic and L-mode plasmas $L_{pol} \sim L_{rad} \sim 4$–7 cm independent of radius, while for H-mode plasmas the scale lengths increased to ~9–10 cm at $\rho = -2$ cm. Figure 6(*c*) shows that the poloidal and radial scale lengths were within a factor-of-two of each other for almost all shots in the database, but with a slight poloidal elongation for points outside the separatrix. Turbulence scale lengths similar to the $\rho = +2$ cm data in figure 6(*c*) were obtained at $\rho = 0$ cm and $\rho = +4$ cm.

Figure 6(*d*) shows that L_{pol} increases with plasma stored energy W_{mhd}, apparently with a change across the Ohmic to H-mode boundary shown by the vertical line (similar results are obtained for L_{rad}). Figure 6(*e*) shows L_{rad} decreasing with increased plasma current I_p at $\rho = -2$ cm, although L_{pol} is independent of I_p at this radius. Finally, figure 6(*f*) shows a slightly increasing L_{pol} with local edge T_e at $\rho = 0$ cm, but with considerable scatter.

Table 4 showed linear (pair-wise) correlation coefficients between L_{pol} and L_{rad} and several parameters in this database for $\rho = \pm 2$ cm. Fairly strong correlations occur between L_{pol} and line-averaged density (n_e-ave), neutral beam power P_{nb}, stored plasma energy W_{mhd}, lithium per shot, and edge n_e, although these are also correlated with each other. Table 4 also shows a moderate (0.53) correlation between the L_{pol} and the plasma elongation κ. Table 5 shows the power-law exponents for the entries of table 4. The poloidal correlation length increases with W_{mhd}, n_e-ave and edge n_e with a power law exponent ~0.4 ± -0.1, and the power law exponent for κ was a high 2.9.

4.2. Blob scale lengths

The radial profiles of the blob poloidal and radial scale lengths are shown in figures 7(*a*) and (*b*), with error bars giving the shot-to-shot standard deviations. The blob poloidal scales were L_{pol} ~3–4 cm for Ohmic and L-mode plasmas and L_{pol} ~4–5 cm for H-mode plasmas, and the blob radial scales were L_{rad}~2–3 cm at or outside $\rho = 0$ cm, and L_{rad}~3–4 cm at $\rho = -2$ cm. Figure 7(*c*) shows the blob scale lengths L_{pol} and

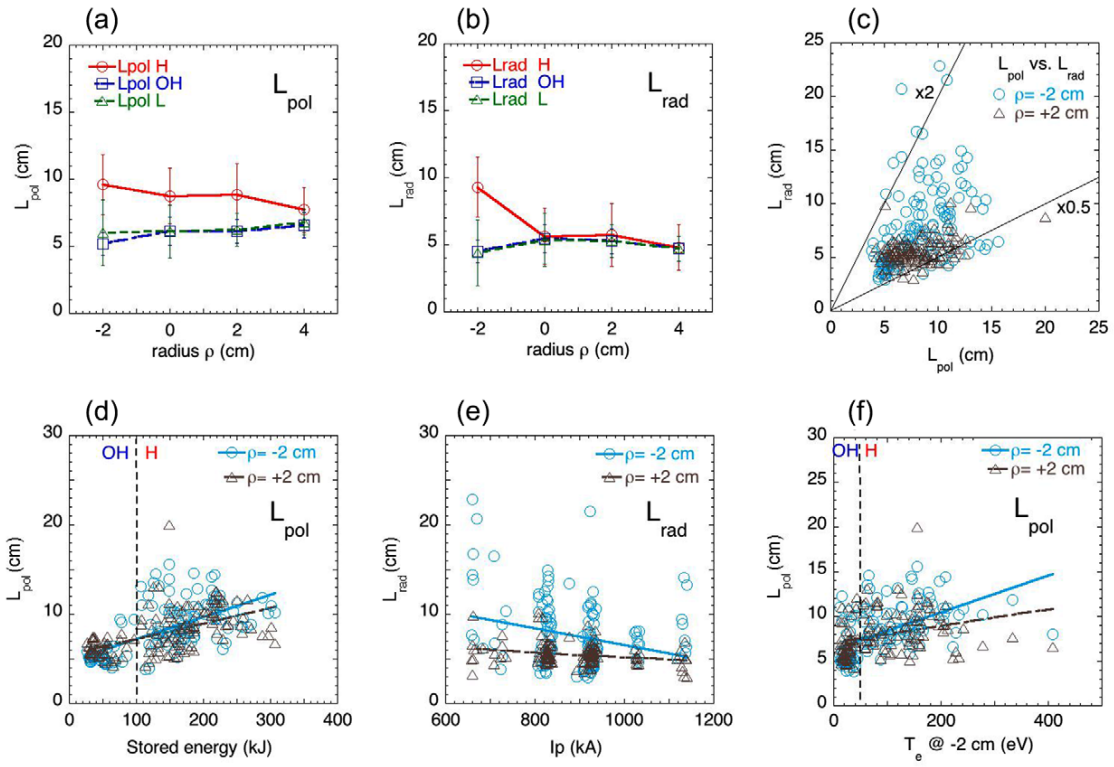

Figure 6. (*a*) and (*b*) show radial profiles of the turbulence correlation lengths L_{pol} and L_{rad}, sorted according to shot type. (*c*) shows the turbulence L_{pol} versus L_{rad} for all shots in the database at $\rho = \pm 2$ cm. (*d*)–(*f*) show the turbulence L_{pol} versus the plasma stored energy, the turbulence L_{rad} versus the plasma current, and the turbulence L_{pol} versus the edge temperature, all at $\rho = \pm 2$ cm.

L_{rad} for the entire database at $\rho = 0$ cm and +4 cm, which tend to be nearly a factor-of-two longer in the poloidal direction.

Figure 7(*d*) shows an example of blob variations; in this case, the blob L_{pol} is nearly constant versus plasma current at $\rho = 0$ cm and +4 cm. No other significant variations of blob scale lengths with plasma parameters were found, e.g. with line-averaged density, toroidal field, or lithium coating. Figures 7(*e*) shows that the blob L_{pol} tend to be somewhat lower than the turbulence L_{pol} (section 4.1), and figure 7(*f*) shows that the blob L_{rad} were also somewhat lower than the turbulence L_{rad}.

4.3. Turbulence scale lengths versus theory

Edge turbulence scale lengths are presumably set by the nonlinear evolution of drift-waves and/or interchange modes driven by temperature and/or density gradients [17, 26, 29]. The analysis below is meant to explore the character of the turbulence scale lengths in the region inside the separatrix. Although the blob algorithm can track the motion of positive structures in this region, the scale length of the blobs were judged to be less relevant for this analysis than the scale lengths of the turbulence as a whole. Hence, the turbulence scale lengths L_{rad} and L_{pol} from the correlation analysis were employed.

Figure 8(*a*) shows a comparison of the poloidal turbulence scale lengths of section 4.1 with the generic drift-wave gyroradius scale $\rho_s = 10^2(M_i T_e)^{1/2}/Z_i B_t$, where B_t is taken as the field at the magnetic axis, L_{pol} is measured at $\rho = -2$ cm, $M_i = 2$ and $Z_i = 1$ for the main deuterium ions, and the T_e is from the Thomson scattering $\rho = -2$ cm. Dashed lines are shown for two values of $k_{pol}\rho_s$, where we assume $k_{pol} = 2/L_{pol}$. The data in figure 8(*a*) are best fit by $k_{pol}\rho_s \sim 0.06$ (or $k_{pol}\rho_s \sim 0.12$ using the outer separatrix B), which corresponds to a poloidal scale length a few times larger than expected from linear drift-wave instabilities at $k_{pol}\rho_s \sim 0.3$. The larger size scales measured in H-mode shots are at least qualitatively consistent with the larger drift-wave gyroradius scale in those shots, although there is a factor-of-two scatter in $k_{pol}\rho_s$. Note that there may be a significant component of carbon ions in the region 2 cm inside the separatrix with $M_i = 6$ and $Z_i \sim 2$, which is not taken into account in this comparison.

The theory of interchange modes predicts a broad spectrum of instability up to the radial size scale of the pressure gradient [28, 29]. Figure 8(*b*) shows a comparison of the radial turbulence length L_{rad} with the pressure scale length L_p from Thomson scattering, both evaluated at $\rho = -2$ cm. For Ohmic shots this relationship is $L_{rad} \sim (2\text{–}4)L_p$, but for H-mode shots $L_{rad} \sim (5\text{–}15)L_p$. Thus the radial scale length of the turbulence in Ohmic plasmas at 2 cm inside the separatrix is similar to that expected from the interchange scale length, but for H-mode plasmas it is significantly larger than expected. This relationship could not be tested at larger radii since the local pressure gradient scale lengths were not well known there.

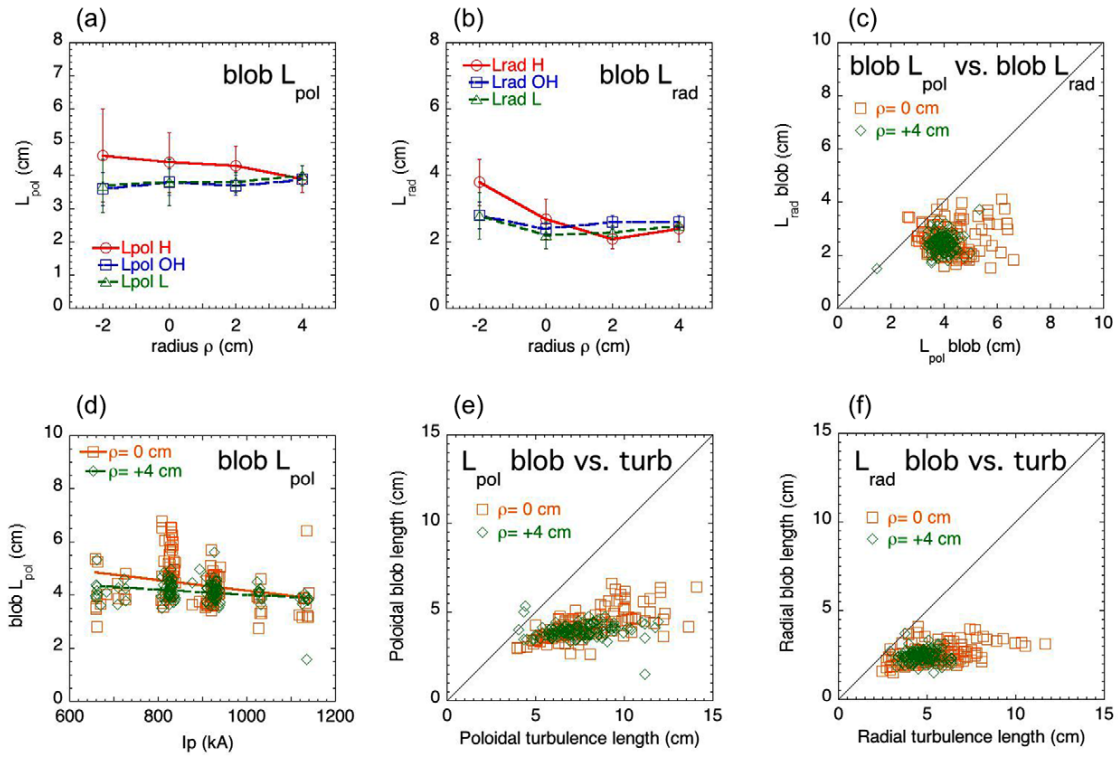

Figure 7. (*a*) and (*b*) show radial profiles of the blob scale lengths L_{pol} and L_{rad}, sorted according to shot type. (*c*) shows the blob L_{pol} versus the blob L_{rad} for all shots in the database at $\rho = 0$ cm and +4 cm. (*d*)–(*f*) show the blob L_{pol} versus the plasma current, the blob L_{pol} versus the turbulence L_{pol}, and the blob L_{rad} versus the turbulence L_{rad}, all at $\rho = 0$ cm and +4 cm.

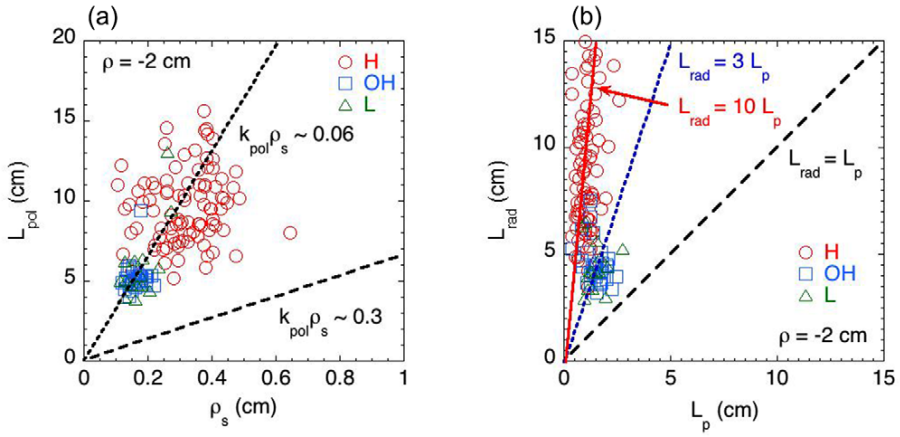

Figure 8. Comparison of the measured length scales of the turbulence at $\rho = -2$ cm with simplified theoretical models. In (a) the poloidal correlation lengths L_{pol} are compared with the drift-wave gyroradius parameter ρ_s, showing a best fit to $k_{pol}\,\rho_s \sim 0.06$ (using the magnetic field on axis for *B*). In (b) the measured radial correlation lengths L_{rad} at $\rho = -2$ cm are compared with the radial pressure gradient scale length L_p, which is a scale expected from interchange turbulence. The best fits are $L_{rad} \sim 3L_p$ for Ohmic and L-mode plasmas and $L_{rad} \sim 10L_p$ for H-mode plasmas.

4.4. Comparison with previous experiments

Beam emission spectroscopy measurements of edge turbulence in H-modes in NSTX [31, 32] showed poloidal correlation lengths of $L_{pol} \sim 10$–20 cm, which is near to the $L_{pol} \sim 10$ cm measured at $\rho = -2$ cm in H-modes shown figure 6(*a*). Parameter scalings in this BES data included an increase in L_{pol} with d*n*/d*r*, whereas GPI data for H-modes at $\rho = -2$ cm did not show significant trends in these directions. Langmuir probe measurements in L-modes and H-modes in NSTX [34] showed poloidal and radial correlation lengths of $L_{pol} \sim 4$–9 cm and $L_{rad} \sim 2$–6 cm, similar to figures 6(*a*) and (*b*). However, reflectometer measurements in the steep density gradient region between ELMs [43] were consistent with a radial correlation length of $L_{rad} \sim 2$ cm (FWHM), which is significantly

lower than at the GPI results at $\rho = -2$ cm for H-modes in figure 6(*b*).

Previous turbulence results from tokamaks generally found a poloidal size scaling $k_{pol}\rho_s \sim 0.02$–0.1 [4–8], similar to the results of figure 8(*a*). A recent cross-machine database [11] found $L_{pol} \sim \rho_s^{0.55}$, whereas the present database was well fit by $L_{pol} \sim 33\rho_s$. Imaging of the edge blobs (a.k.a. filaments) in MAST at similar B to NSTX [44] showed $L_{pol} \sim 7$–12 cm and $L_{rad} \sim 3$–10 cm, similar to the blob scales of figures 7(*a*) and (*b*). The GPI diagnostic on Alcator C-Mod showed correlation lengths $L_{pol} \sim L_{rad} \sim 1$ cm [37], which are about ten times smaller than NSTX, most likely due to the ×10 higher toroidal field through the gyroradius scaling.

In early ASDEX Ohmic discharges [45], the poloidal correlation length in the SOL increased with increased density, whereas here the turbulence L_{pol} at $\rho = +2$ cm and +4 cm decreased with increased density (not shown). In Alcator C-Mod [46, 47] the size of blobs measured by GPI in the SOL varied little with discharge parameters, similar to the present results. Tokamak blob sizes cited in a recent review [10] ranged from ~1–8 cm (FWHM), which are within or near the range shown in figure 7.

A recent study of blobs done in the SOL of L-mode plasmas in ASDEX Upgrade with Li-BES [41] found a radial size $L_{rad} \sim 2$–8 cm (FWHM), similar to the NSTX blob results of figure 7(*b*). The poloidal blob size (half-width) in the SOL of ASDEX Upgrade were also recently measured with GPI to be $\delta_b \sim 7$ mm in L-mode and ~8 mm in H-mode [42], which is about 2–3 times smaller than the NSTX blob (full-width) $L_{pol} \sim 3$–5 cm shown in figure 7(*a*). This is roughly consistent with a $k_{pol}\rho_s \sim$ constant (drift-wave) scaling, since the B field in ASDEX Upgrade (2.5 T) was ~5 times larger than the average B field of NSTX for this database (0.45 T).

5. Turbulence and blob poloidal velocity

This section describes the edge and SOL turbulence and blob poloidal velocities V_{pol} for this database. Section 5.1 describes the V_{pol} derived from cross-correlation analysis. Section 5.2 describes the V_{pol} for the blob structures. Section 5.3 discusses theoretical interpretations, and section 5.4 describes the relationship of these results to previous experiments.

5.1. Turbulence poloidal velocity

Figure 9(*a*) shows the radial profile of the turbulence poloidal velocity V_{pol}, sorted versus discharge type, along with shot-to-shot error bars. Typically $V_{pol} \sim -2 \pm 1$ km s^{-1} in the ion diamagnetic and grad-B drift poloidal drift direction (i.e. downwards in NSTX), except for a clear reversal to an electron diamagnetic velocity for Ohmic plasmas at $\rho = -2$ cm, to $V_{pol} \sim +3.5 \pm 2$ km s^{-1}. In the SOL, V_{pol} tends to get closer to zero at larger radii for all discharge types.

It is important to determine if the turbulence V_{pol} varies with the NBI power P_{nb}, since the turbulence velocity should depend on the plasma velocity, and the beams in NSTX are injected in the co-current toroidal direction. However, figure 9(*b*) shows that there is little or no systematic change in V_{pol} with P_{nb}, except for the change across the Ohmic-to-H mode boundary for $\rho = -2$ cm; a similar trend was found when V_{pol} was plotted versus W_{mhd} (not shown). An attempt was made to compare the edge turbulence V_{pol} with the edge velocity measured using Doppler shifts of the passively-observed CIII triplet (~465 nm) located at 2.4 ± 1.9 cm inside the separatrix. However, the poloidal velocity of CIII was largely in the opposite direction from the turbulence V_{pol} at $\rho = -2$ cm, and the V_{tor} from CIII was in the opposite toroidal direction expected from NBI-induced rotation. Thus it unclear whether the CIII rotation data is representative of the plasma edge fluid rotation in these experiments.

Figure 9(*c*) shows that there is little or no systematic change in V_{pol} with T_e, except for the change from Ohmic-to-H mode boundary at $\rho = -2$ cm, and a similar result was found when V_{pol} was plotted versus grad P_e (not shown). This is somewhat surprising since these parameters affect the diamagnetic drift velocity; the relationship of V_{pol} to the diamagnetic drift speed is discussed in section 5.3.

The turbulence V_{pol} was highly (>0.5) correlated with several plasma parameters as shown in table 4, namely P_{nb}, W_{mhd}, line-averaged density (n_e-ave), lithium per shot, and edge n_e. As mentioned in section 4.1, these parameters are also highly correlated with each other, so their causal relationship with the turbulence V_{pol} is unclear.

5.2. Blob poloidal velocity

The radial profile of the blob poloidal velocity as shown in figure 9(*d*) is similar to the radial profile of the turbulence poloidal velocity shown in figure 9(*a*). In particular, the blob poloidal velocity also reverses to the electron diamagnetic direction for Ohmic plasmas at $\rho = -2$ cm, but with a somewhat lower positive velocity. The blob V_{pol} variation with P_{nb} as shown in figure 9(*e*) is also similar to the turbulence variation with P_{nb} in figure 9(*b*), with little or no change in blob V_{pol} with P_{nb}. A direct comparison of the blob V_{pol} with the turbulence V_{pol} for $\rho = 0$ and +4 cm is shown in figure 9(*f*). The poloidal turbulence and blob velocities were generally similar to each other at the $\rho = 0$ cm and +4 cm points, as well as the $\rho = +2$ cm point (not shown).

5.3. Turbulence poloidal velocity versus theory

The poloidal velocity of the turbulence should be the sum of the turbulence velocity in the plasma rest frame plus the poloidal velocity of the plasma (e.g. due to toroidal rotation of field-aligned structures), both of which can be in either direction for various edge rotation directions and/or edge instabilities.

A toroidal plasma rotation in the direction of NBI should cause an apparent poloidal motion of field-aligned edge filaments in the negative (ion diamagnetic) direction with $V_{pol}(\text{NBI}) \sim (B_{pol}/B_{tor})V_{tor} \sim V_{tor}$, which is consistent with the measured direction of the turbulence V_{pol} with NBI in H-mode. However, since the CIII rotation data was not in this toroidal

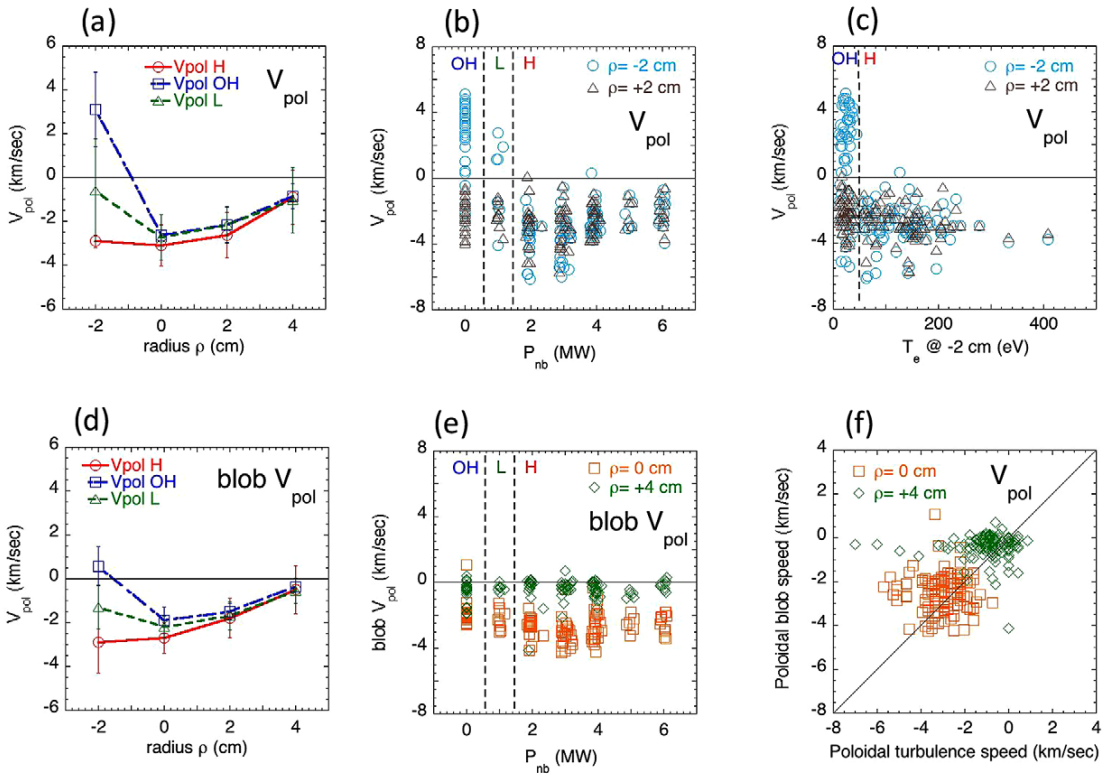

Figure 9. (*a*) show the radial profile of the poloidal turbulence velocity V_{pol}, sorted according to discharge type. (*b*) and (*c*) show the turbulence V_{pol} versus the neutral beam power and edge T_e for $\rho = \pm 2$ cm, with dashed lines indicating the range of discharge types. (*d*) shows the radial profile of the blob velocity V_{pol}, sorted according to discharge type. (*e*) shows the blob V_{pol} versus the neutral beam power and (*f*) shows the blob V_{pol} versus the turbulence V_{pol}, both for $\rho = 0$ cm and +4 cm.

direction (see section 5.1), it will not be used to interpret the measured V_{pol}. The observed direction of the turbulence velocity in the SOL is consistent with the expected sign of the radial electric field associated with the connection to the divertor sheath.

The calculated diamagnetic drift speed evaluated at $\rho = -2$ cm is compared with the poloidal velocity of the turbulence in figure 10(*a*). The diamagnetic drift speed is taken to be $V_{drift} = \pm c_s \rho_s / L_n$, where L_n is the density gradient scale length and ρ_s is evaluated using the magnetic field on axis and T_e at $\rho = -2$ cm. The Ohmic plasmas have a velocity $V_{pol} \sim (1\text{–}3) V_{De}$, roughly consistent with an electron drift wave. However, the H-mode plasmas have $V_{pol} \sim (0.2\text{–}1) V_{Di}$, which is in the opposite direction and smaller than the ion diamagnetic velocity. Thus the reversal in V_{pol} for Ohmic plasmas may be due the dominance of the electron drift wave propagation in those plasmas with relatively little NBI-induced rotation.

5.4. Comparison with previous experiments

The poloidal velocity of the turbulence seen in H-modes by BES in NSTX was $V_{pol} \sim -5$ km s^{-1} [28], which is similar to the $V_{pol} \sim -3$ km s^{-1} seen for H-modes in figure 9(*a*). The poloidal turbulence velocity inferred from Langmuir probes in NSTX [34] was $V_{pol} \sim +10$ km s^{-1} at $\rho = -2$ cm and $V_{pol} \sim -2$ km s^{-1} at $\rho = +2$ cm, at least qualitatively similar to the reversal seen in GPI results for Ohmic plasmas in figure 9(*a*). The reversal of the poloidal velocity versus radius in Ohmic plasmas was first seen in TEXT [48].

Filaments in MAST H-modes were also seen to rotate toroidally in the co-current direction $V_{tor} \sim 8 \pm 3$ km s^{-1} [36], which implies a $V_{pol} \sim -5$ km s^{-1}, which is similar to the blob speeds in figure 9(*b*). The GPI diagnostic on Alcator C-Mod shows similar poloidal turbulence velocities as NSTX [37], and the dual GPI diagnostic on EAST [49] showed a reversal in the average V_{pol} direction across the separatrix, similar to that the Ohmic shots here in figure 9(*a*). In ASDEX Ohmic discharges, the poloidal velocity decreased with increased density [45], whereas here V_{pol} at $\rho = +2$ cm and +4 cm increased with density, opposite to ASDEX. The poloidal velocity of blobs in the SOL was measured recently using GPI in ASDEX Upgrade to be $V_{pol} \sim 0.1\text{–}0.3$ km s^{-1} [42], which is generally less than the results in figure 9(*d*), and the poloidal blob velocity reversed from the Ohmically heated L-mode phase to H-mode, similar to the results for NSTX inside the separatrix in figure 9(*b*).

6. Turbulence and blob radial velocity

This section describes the edge and SOL turbulence and blob radial velocities V_{rad} for this database. Section 6.1 describes the V_{rad} derived from cross-correlation analysis. Section 6.2 describes the V_{rad} for the blob structures. Section 6.3 discusses

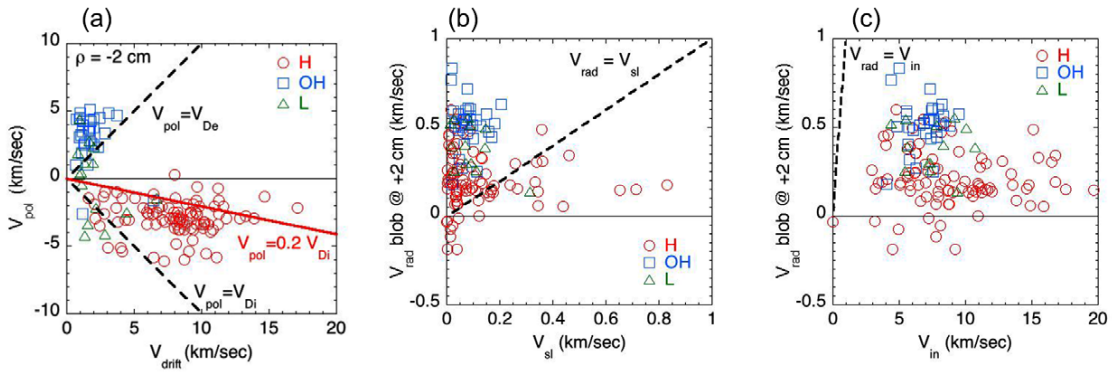

Figure 10. (*a*) is a comparison of the poloidal velocity of the turbulence at $\rho = -2$ cm versus the calculated ion and electron diamagnetic drift speeds, using B on axis. (*b*) and (*c*) are comparisons of the measured radial blob velocity at 2 cm outside the separatrix with calculated blob velocities based on the sheath-limited velocity and the inertial range velocity, using B on axis for ρ_s.

theoretical interpretations, and section 6.4 describes the relationship of these results to previous experiments.

6.1. Turbulence radial velocity

The radial profile of the turbulence radial velocities V_{rad} is shown in figure 11(*a*), where these velocities are derived from the time-delayed cross-correlation analysis as described in section 2.4. These shot-averaged V_{rad} are all outwards and between 0.1–1 km s^{-1}, but are somewhat lower for H-mode plasmas in the region $\rho \geqslant 0$ cm. An example of the variation of V_{rad} with plasma parameters is shown in figure 11(*b*). There is significant scatter in the results over the database of individual shots, including some negative values, but there is little or no systematic variation of V_{rad} with P_{nb} at $\rho = \pm 2$ cm. There were no significant cross-correlations between the turbulence V_{rad} and the various global and local plasma variables, as shown in table 4.

The relationship between the turbulence V_{rad} and V_{pol} for $\rho = \pm 2$ cm is shown in figure 11(*c*). The majority of shots have a negative V_{pol} and positive V_{rad} with $V_{pol} \gg V_{rad}$ (note the different velocity scales in the figure). However, there was no significant cross-correlation between these two velocities, i.e. the poloidal velocity seems independent of the radial velocity. The relationship between the turbulence V_{rad} and V_{pol} for the $\rho = 0$ cm and +4 cm points was similar to that shown in figure 11(*c*).

6.2. Blob radial velocity

The radial profile of the blob radial velocity is shown in figure 11(*d*). These blob velocities are the average over individual blob radial speeds, as described in section 2.4. These shot-averaged radial velocities are all outwards between 0.1–1 km s^{-1}, and are similar for all plasma types in the region $\rho \geqslant 0$ cm. Figure 11(*e*) shows a general decrease in blob V_{rad} with increasing T_e, although there is considerable scatter in the results. The relationship of the blob V_{rad} to the turbulence V_{rad} is shown in figure 11(*f*). These magnitudes of these velocities are also similar to each other, although they are not well correlated with each other.

6.3. Blob radial velocity versus theory

The radial velocity of the turbulence and blobs in the SOL is of special interest since it determines (at least in part) the width of the heat flux deposition on the divertor plates, and the heat load and impurity generation from midplane vessel structures. There are simple analytic models for the blob radial velocity which can be compared with this database.

Figures 10(*b*) and (*c*) showed a comparison between the measured radial blob velocity at $\rho = +2$ cm with calculated blob velocities based on two different models [17]: with the sheath-limited velocity: $V_{sl} = c_s(L_{II}/R)(\rho_s/\delta_b)^2\ (\delta n/n)$ in figure 10(*b*), and the inertial range velocity: $V_{in} = c_s(\delta_b/R)^{1/2}(\delta n/n)^{1/2}$ in figure 10(*c*). For these plots c_s and ρ_s are the sound speed and drift-wave gyroradius evaluated within ± 1 cm of the separatrix using T_e from Thomson scattering and B on axis,) L_{II} is the parallel connection length to the divertor taken to be 4.5 m with $R = 150$ cm, δ_b is the blob radius taken to be half the measured blob L_{pol} from section 4 and $\tilde{n}/n$ is taken to the normalized amplitude of the blobs at $\rho = +2$ cm outside the separatrix. Note that each point represent the average of many blobs in that radial region for that shot.

The measured radial blob velocities of $V_{rad} \sim 0.3 \pm 0.2$ km s^{-1} are generally higher than the calculated sheath-limited velocity V_{sl} (which average ~0.1 km s^{-1}), but lower than the calculated inertial range velocity V_{in} (which average ~10 km s^{-1}). This is consistent with the previous result that the SOL blobs in NSTX lie between these two regimes [17]. However, there does not appear to be any consistent linear correlation of these calculated velocities with the measured velocities in this database. Both the sheath-limited and inertial range scalings were seen more clearly in an open field line device TORPEX [50].

6.4. Comparison with previous results

Langmuir probe measurements in L-modes and H-modes in NSTX [34] showed radial blob speeds $V_{rad} \sim 1$–4 km s^{-1} in the SOL, higher than the results from figure 11(*b*). Radial blob velocities in MAST were $V_{rad} \sim 0.5$–2 km s^{-1} [36], similar to the blob radial speeds in figure 11(*b*).

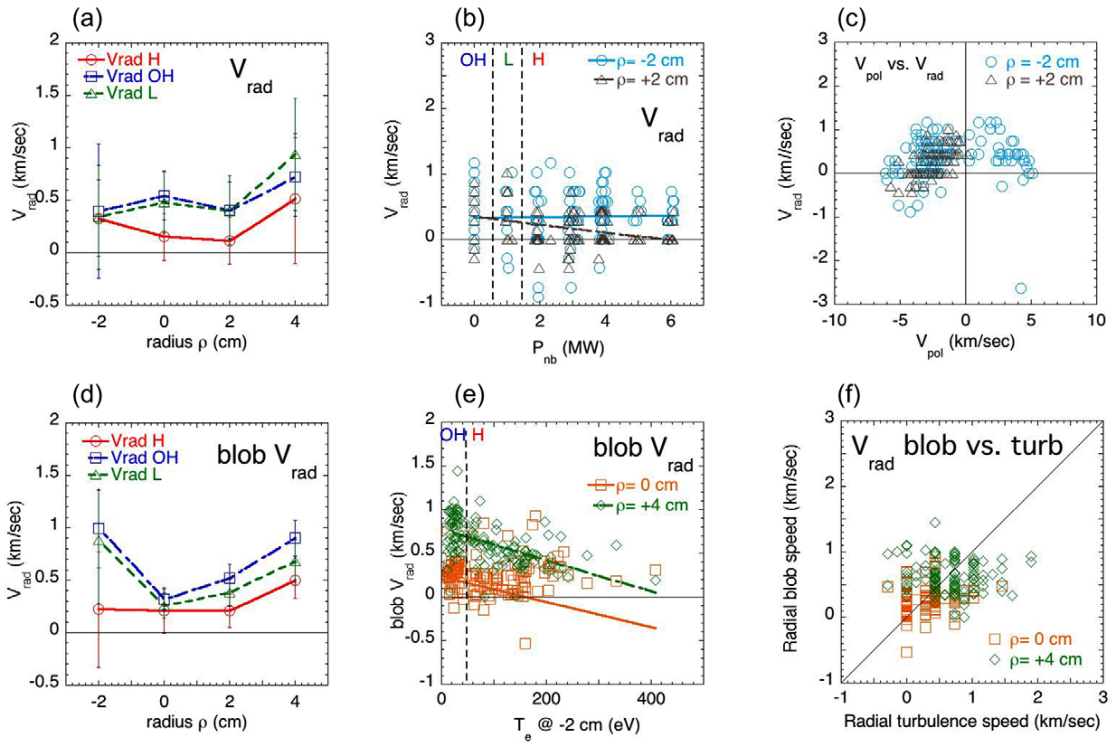

Figure 11. (*a*) shows the radial profile of the turbulence radial velocity V_{rad}, sorted according to discharge type. (b) shows the turbulence V_{rad} versus the neutral beam power and (c) shows the turbulence V_{rad} versus the turbulence V_{pol}, both for $\rho = \pm 2$ cm. (d) shows the radial profile of the blob radial velocity V_{rad}, sorted according to discharge type. (e) shows the blob V_{rad} versus the edge T_e, and (f) shows the blob V_{rad} versus the blob V_{pol}, both for $\rho = 0$ cm and +4 cm.

Tokamak radial blob speeds cited in a recent review [10] ranged from $V_{rad} \sim 0.2$–3 km s^{-1}, which are within the range shown in figure 11, and were bounded by the inertial and sheath-limited models, as they were in figures 10(*b*) and (*c*). Radial blob speeds from a multi-machine database [11] were outwards and mainly within $V_{rad} \sim 0$–3 km s^{-1}, similar to the $V_{rad} \sim 0$–1 km s^{-1} of figure 9(*f*).

Blobs in the SOL of L-mode plasmas in ASDEX Upgrade measured by Li-BES had a mean outward radial velocity in the SOL of ~0–0.2 km s^{-1} [41], similar to the NSTX blob results of figure 1. The radial blob speeds in the SOL of ASDEX Upgrade measured by GPI were only slightly smaller in H-mode than L-mode [42], similar to figure 11(*d*). Radial blob speeds measured with a ball-pen probe in the SOL of ASDEX Upgrade were ~0.5 km s^{-1} [27].

The effective radial convection velocity in the SOL, i.e. the radial particle flux divided by the local density, has been measured using Langmuir probes in TCV to be ~0.15 km s^{-1}, and agreed well with ESEL simulations [51, 52]. Although this velocity is similar to the V_{rad} found for turbulence and blobs in NSTX, the GPI results cannot be used to infer the radial particle convection.

7. Turbulence and blob timescales

The radial profile of the turbulence autocorrelation time τ_{auto} is shown in figure 12(*a*), sorted according to discharge type, with shot-to-shot error bars. These increased with radius from $\tau_{auto} \sim 15$ to ~40 μs for all shot types. The autocorrelation time over the entire database was fairly highly correlated with NBI power, stored energy, and line-average density, as shown in table 4, but not well correlated with I_p (or B_t).

Figure 12(*b*) shows that most τ_{auto} are near $\tau_{pol} = L_{pol}/V_{pol}$ (straight lines), which is the time for turbulence to move past a fixed point when $V_{pol} \gg V_{rad}$. Thus for example, the increase in τ_{auto} at $\rho = +4$ cm in figure 12(*a*) is mostly due to the decrease in V_{pol} there, as shown in figure 9(*a*). About half of the data points are near $\tau_{pol} \sim \tau_{auto}$, indicating significant 'frozen flow' in the poloidal direction, but about half have $\tau_{auto} < \tau_{pol}$, indicating that the turbulence can also change before being convected by the poloidal flow over a poloidal correlation length. This relationship is largely true even for the Ohmic points with positive V_{pol} at $\rho = -2$ cm.

The total blob lifetime for each shot was also evaluated from blob tracking over the entire region of the GPI images in figure 1. These blob lifetimes are compared with the turbulence autocorrelation times at $\rho = \pm 2$ cm in figure 12(*c*). The blob lifetimes are similar to autocorrelation times, although not highly correlated with either of them. The blob lifetime is determined in part by the radial blob motion and also by the evolution of the blob amplitude versus time, as well as the blob convection in the poloidal direction. There are specific predictions about blob dynamics from simulation codes, e.g. that a blob is expelled radially when the poloidal motion stops. However, the dynamics of individual blobs is beyond

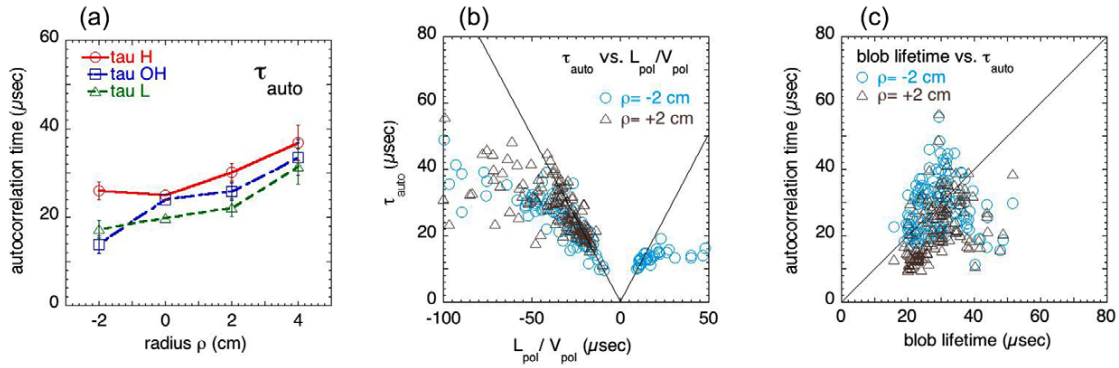

Figure 12. (*a*) shows the radial profile of the turbulence autocorrelation time τ_{auto}, sorted according to discharge type. (*b*) shows the turbulence τ_{auto} versus the turbulence L_{pol}/V_{pol} for $\rho = \pm 2$ cm, indicating near-frozen poloidal flow for much of the database. (*c*) shows the relationship between the total blob lifetime and the turbulence τ_{auto} at $\rho = \pm 2$ cm.

the scope of this paper, and will be treated in a separate publication.

The edge and SOL autocorrelation times $\tau_{auto} \sim 10$–40 μs of figure 12(*a*) are similar to those found in many previous tokamak experiments [4–8], and autocorrelation times in a recent multi-machine database were in the range ~4–40 μs. Blob lifetimes in MAST in H-mode were ~50–120 μs [44], somewhat longer than those shown in figure 12(*c*).

8. Multiple linear regression analysis

Standard multiple linear regression analysis (MLR) was applied to the entire database to fit the turbulence quantities with simultaneous products of power laws of the global and local plasma parameters. In principle, this process could find improved fits with respect to the single-parameter cross-correlations shown in tables 4 and 5. The turbulence variables used were $\delta I/I$, τ_{auto}, L_{pol}, and L_{rad} from the cross-correlation analysis (V_{pol} and V_{rad}, were not used since they had both negative and positive values). The fit parameters initially chosen as independent variables were I_p, B_t, line-averaged n_e, lithium/shot, stored energy W_{mhd}, κ, edge n_e, edge dn_e/dR, q_{sep}, and the edge V_{tor} from the CIII measurements.

Table 6 shows the most statistically significant dependences found from this MLR analysis for the turbulence at $\rho = \pm 2$ cm. In each box are the power law exponents; for example, the most significant dependences for the relative fluctuation level at $\rho = -2$ cm are $\delta I/I \sim (B_t)^{-0.88\pm0.31}(dn_e/dR)^{-0.15\pm0.06}$. The significance and influence of the various independent variables on the overall regression fit was determined by examining the results of the f- and t-tests. All entries for the cases presented in table 6 were significant at the 95% confidence level. By examining several representative cases, we found that by removing the least statistically significant variables ($\leqslant$25% confidence level) did not change the most significant fit coefficients (shown in table 6), to within their standard errors.

Some of the stronger dependences of table 6 are similar to those found from the single-variable correlations of table 5. For example, $\delta I/I \sim B_t^{-0.88\pm0.31}$ in table 6 and $\delta I/I \sim B_t^{-1.7\pm0.29}$ in table 5 ($\rho = -2$ cm), $\tau_{auto} \sim n_e^{0.45\pm0.14}$ in table 6 and $\tau_{auto} \sim n_e^{0.62\pm0.05}$ in table 5 ($\rho = +2$ cm), and $L_{pol} \sim \kappa^{1.43\pm0.41}$ in table 6 and $L_{pol} \sim \kappa^{2.92\pm0.04}$ in table 5 ($\rho = -2$ cm). However, some dependences found to be significant in the MLR, e.g. the I_p dependence of τ_{auto} and L_{pol}, did not have high (>0.5) single-variable correlations, for reasons which are not yet clear.

The results of the MLR analysis of table 6 can be compared with the theoretical expectations discussed in sections 3.3 and 4.3. The relative fluctuation level from the mixing length model is expected to vary as $\delta I/I \sim (dn_e/dr)^{-1}$, whereas the MLR scaling is much weaker, i.e. $\delta I/I \sim (dn_e/dr)^{-0.15\pm0.06}$. This inconsistency was also seen in figure 5, where the H-mode data did not follow the mixing length expectation. The poloidal correlation lengths from drift wave scaling are expected to vary as $L_{pol} \sim B_t^{-1}$, which is similar to the $L_{pol} \sim B_t^{-0.80\pm0.30}$ scaling of the MLR for $\rho = +2$ cm but was not seen at $\rho = -2$ cm. There is no clear theoretical interpretation at present for the relatively strong MLR scalings of $\tau_{auto} \sim I_p^{0.97\pm0.24}$ or $\tau_{auto} \sim n_e^{0.41-0.45}$. The strong MLR scaling of $L_{pol} \sim \kappa^{1.43-1.52}$ seems to suggest a strong flux-surface shaping effect L_{pol}, which is surprising (this was not due to a correlation of L_{pol} or κ with the B-field line angle in the GPI field of view). However, since the range of κ was only $\kappa \sim 1.9$–2.5, an exponent of 1.5 implies a variation of only ×1.5 over the database.

In general, this MLR analysis did not provide a clear or theoretically plausible empirical scaling for the variations of the edge turbulence across this database. This may point to the need to include more relevant local physics parameters in the database, such as those which determine the L–H transition and/or SOL width (which have not yet been identified theoretically). The tentative conclusion is that the observed variations are not yet well understood.

9. Conclusions

This paper described edge and SOL turbulence in NSTX using a large database which covered most of the operational range of the machine. The specific goals were to determine how the turbulence varied with the global and local plasma parameters and how well these turbulence variations could be described by simplified theoretical models.

Table 6. Multiple linear regression exponents for turbulence quantities.

	radius	I_p	B_t	n_e-ave	Li/shot	W_{mhd}	κ	dn_e/dR
$\delta I/I$	−2 cm	—	−0.88 ± 0.31	—	—	—	—	−0.15 ± 0.06
	+2 cm	—	—	−0.22 ± 0.07	—	—	—	—
τ_{auto}	−2 cm	—	—	0.45 ± 0.14	—	—	—	—
	+2 cm	0.97 ± 0.24	—	0.41 ± 0.13	—	—	—	—
L_{pol}	−2 cm	−0.62 ±.20	—	—	—	—	1.43 ± 0.41	—
	+2 cm	—	−0.80 ± 0.30	—	—	—	1.52 ± 0.44	—
L_{rad}	−2 cm	—	—	—	0.08 ± 0.02	—	—	—
	+2 cm	—	—	—	0.04 ± 0.01	0.25 ± 0.08	1.73 ± 0.34	0.17 ± 0.05

There were clear variations in the turbulence with respect to the minor radius; for example, with increased distance into the SOL the fluctuation levels increased (figure 3), the poloidal velocities decreased (figure 9), the radial velocities increased (figure 11), and the autocorrelation times increased (figure 12). On the other hand, both the turbulence and blob correlation lengths were independent of radius to within ±10% for $\rho = 0$, 2 and 4 cm for each discharge type (figures 6 and 7), although the radial correlation lengths were up to a factor of 2 larger for $\rho = -2$ cm in H-mode plasmas.

Some clear relationships were found between turbulence quantities across the whole database. For example, the poloidal and radial correlation lengths were usually within a factor-of-two of each other (figures 6 and 7), so the blobs have an almost circular cross-section. The autocorrelation time was near the poloidal correlation length divided by the poloidal velocity (figure 12), so the timescales were similar to that expected for frozen-flow in the poloidal direction. In general, the blob tracking results were consistent with the turbulence correlation results. For example, the normalized blob amplitude increased linearly with the relative fluctuation level (figure 4), the blob lengths were similar to the turbulence correlation lengths (figures 7), the blob poloidal speeds were similar to the poloidal correlation speeds (figure 9), and the blob lifetime was similar to the autocorrelation time (figure 12).

Systematic variations in the turbulence were found with various global and local plasma parameters; for example, the relative turbulence fluctuation level decreased with increasing line-averaged density, increasing stored plasma energy, and increasing edge electron temperature, as shown in figure 3. However, these plasma parameters were also correlated with each other, so it was not possible to identify a unique plasma parameter which controlled the turbulence variations. This is not too surprising, since the ultimate cause of both these turbulence variations and plasma variations will most likely be found using theoretical models of the underlying plasma instabilities.

With respect to the simplified theoretical models, the poloidal scale lengths were fairly well described by $k_{pol}\rho_s \sim 0.06$ (figure 8), which at least qualitatively explains the larger scale lengths in H-mode (i.e. hotter) plasmas. The relative fluctuation levels in Ohmic and L-mode plasmas were close to the wave breaking limit $\delta n/n \sim 1/k_{rad}L_n \sim 0.2$–$0.4$ [53, 54]. but considerably lower than this limit in H-mode plasmas (figure 5). The poloidal velocities were close to the electron diamagnetic drift speed in Ohmic plasmas, but considerably less than the ion diamagnetic speed in H-mode plasmas, and the blob radial speeds at 2 cm outside the separatrix were found to lie between the 'sheath limited' and 'inertial' range speeds (figure 10), as previously found in NSTX [17] and elsewhere [10].

There were several new and/or surprising results with respect to previous studies of edge turbulence. For example, there was no significant increase in the poloidal turbulence velocity with increased NBI power over $P_{nb} \sim 2$–6 MW in H-mode plasmas, despite increases in edge pressure and core toroidal rotation with NBI. The local radial correlation lengths just inside the separatrix in H-mode plasmas were ~2–5 times larger than the local density gradient scale, which seems inconsistent with drift wave theory [53]. There was relatively little variation of the turbulence or blob properties with respect to plasma current or toroidal field, but the MLR analysis did indicate a significant increase in L_{pol} with κ. Although not new [48], there was a surprisingly clear reversal in poloidal turbulence velocity with radius in Ohmic plasmas, consistent with recent results of Alcator C-Mod [55] and TJ-K [56].

We close by pointing out some uncertainties and limitations in the present results which could motivate further work. A major limitation is the lack of density and temperature data in the SOL, which makes connections with turbulence theory difficult. Ideally, the 2D profiles of n_e and T_e should be measured on the timescale of the turbulence, so that the relationship between δn and δT_e should be determined. To gain further understanding of the relevant physical processes, it might also help to correlate the edge turbulence variations with the edge impurity content, SOL flows, and heat flux width at the divertor plate. Turbulence measurements at other poloidal locations are also needed to clarify the 3D structure of the fluctuations, and better cross-diagnostic comparisons would be useful to clarify the systematic uncertainties in each diagnostic.

The present NSTX database was based on many separate experiments done during 2010, which introduced uncontrolled variations in the edge neutral density, impurity levels, and magnetic geometry. This made it more difficult to isolate clear parametric dependences on the other global and local variables. With more systematic scans it might be possible to clarify the effects of parameters such as the plasma current, X-point location, lithium coating, or local gradients on the edge and SOL turbulence.

Finally, the data analysis procedures were kept simple for this large database, and there is still more to learn about the turbulence structure and motion than found in these scale lengths, fluctuation levels, and turbulence velocities.

For example, further analysis could study the (ω,k) spectra, search for zonal flows and counter-propagating waves, identify blob formation, and study the nonlinear couplings in this turbulence.

Acknowledgments

This work was supported by USDOE Contracts DE-AC02-09CH11466 and DE-FG02-02ER54678. We also would like to thank the referees for their helpful comments.

References

[1] Sabbagh S.A. *et al* 2014 *Nucl. Fusion* **53** 104007
[2] Surko C.M. and Slusher R.M. 1983 *Science* **221** 817
[3] Liewer P.C. 1985 *Nucl. Fusion* **25** 543
[4] Wootton A.J. *et al* 1990 *Phys. Fluids* **B 2** 2879
[5] Wagner F. and Stroth U. 1993 *Plasma Phys. Control. Fusion* **35** 1321
[6] Hidalgo C. 1995 *Plasma Phys. Control Fusion* **37** A53
[7] Zweben S.J. *et al* 2007 *Plasma Phys. Control. Fusion* **49** S1
[8] Boedo J. 2009 *J. Nucl. Mater*. **390–391** 29
[9] Krasheninnikov S.I. *et al* 2008 *J. Plasma Phys*. **74** 679
[10] D'Ippolito D.A. *et al* 2011 *Phys. Plasmas* **18** 060501
[11] Simon P. *et al* 2014 *Plasma Phys. Control. Fusion* **56** 095015
[12] Zweben S.J. *et al* 2004 *Nucl. Fusion* **44** 134
[13] Zweben S.J. *et al* 2006 *Phys. Plasmas* **13** 056114
[14] Maqueda R.J. *et al* 2011 *J. Nucl. Mater*. **415** S459
[15] Cao B. *et al* 2012 *Plasma Phys. Control. Fusion* **54** 112001
[16] Zweben S.J. *et al* 2014 *Plasma Phys. Control. Fusion* **56** 095010
[17] Myra J.R. *et al* 2006 *Phys. Plasmas* **13** 092509
[18] Myra J.R. *et al* 2011 *Phys. Plasmas* **18** 012305
[19] Russell D.A. *et al* 2011 *Phys. Plasmas* **18** 022306
[20] Myra J.R. *et al* 2013 *Nucl. Fusion* **53** 073013
[21] PPPL 2015 *Supplementary material* (http://w3.pppl.gov/~szweben/NF2015/NF2015.html)
[22] Cao B. *et al* 2013 *Fusion Sci. Technol*. **64** 29
[23] Davis W.M. *et al* 2014 *Fusion Eng. Des.* **89** 717
[24] Stotler D.P. *et al* 2003 *J. Nucl. Mater*. **313–316** 1066
[25] Zweben S.J. *et al* 2009 *Phys. Plasmas* **16** 082505
[26] Halpern F. *et al* 2015 *Plasma Phys. Control. Fusion* **57** 054005
[27] Horacek J. *et al* 2010 *Nucl. Fusion* **50** 105001
[28] Myra J.R. *et al* 2008 *Phys. Plasmas* **15** 032304
[29] Scott B.D. 2005 *Phys. Plasmas* **12** 062314
[30] Zweben S.J. *et al* 2010 *Phys. Plasmas* **17** 102502
[31] Smith D.R. *et al* 2013 *Phys. Plasmas* **20** 055903
[32] Smith D.R. *et al* 2013 *Nucl. Fusion* **53** 113029
[33] Sechrest Y. *et al* 2015 *Phys. Plasmas* **22** 052310
[34] Boedo J.A. *et al* 2014 *Phys. Plasmas* **21** 042309
[35] Canik J.M. *et al* 2011 *Phys. Plasmas* **18** 056118
[36] Militello F. *et al* 2013 *Plasma Phys. Control. Fusion* **55** 025005
[37] Terry J.L. *et al* 2007 *Fusion Sci. Technol*. **51** 342
[38] Rhodes T.L. *et al* 1993 *Nucl. Fusion* **33** 1147
[39] Boedo J.A. *et al* 2003 *Phys. Plasmas* **10**1670
[40] Antar G.Y. *et al* 2008 *Plasma Phys. Control. Fusion* **50** 095012
[41] Birkenmeier G. *et al* 2014 *Plasma Phys. Control. Fusion* **56** 075019
[42] Fuchert G. *et al* 2014 *Plasma Phys. Control. Fusion* **56** 125001
[43] Diallo A. *et al* 2013 *Phys. Plasmas* **20** 012505
[44] Ben Ayed N. *et al* 2009 *Plasma Phys. Control. Fusion* **51** 035016
[45] Endler M. *et al* 1995 *Nucl. Fusion* **35** 1307
[46] Agostini M. *et al* 2011 *Nucl. Fusion* **51** 053020
[47] Kube R. *et al* 2013 *J. Nucl. Mater*. **438** S505
[48] Ritz Ch. *et al* 1984 *Phys. Fluids* **27** 2956
[49] Shao L.M. *et al* 2013 *Plasma Phys. Control. Fusion* **55** 105006
[50] Theiler C. *et al* 2009 *Phys. Rev. Lett*. **103** 065001
[51] Garcia O.E. *et al* 2007 *Nucl. Fusion* **47** 667
[52] Garcia O.E. *et al* 2005 *Phys. Plasmas* **12** 062309
[53] Horton W. 1999 *Rev. Mod. Phys*. **71** 735
[54] Ricci P. and Rogers B.N. 2013 *Phys. Plasmas* **20** 010702
[55] Cziegler I. *et al* 2010 *Phys. Plasmas* **17** 056120
[56] Nold B. *et al* 2014 *Phys. Plasmas* **21** 102304